Characterization of Alport Syndrome and DPP9 protease using Col4a3 knock-out mice and DPP9 protease dead mutant mice

Inauguraldissertation

zur
Erlangung der Würde eines Doktors der Philosophie
vorgelegt der
Philosophisch-Naturwissenschaftlichen Fakultät
der Universität Basel

von

Munkyung Kim

von South Korea

Basel, 2015

Genehmigt von der Philosophisch-Naturwissenschaftlichen Fakultät

auf Antrag von Prof. Ed Palmer, Prof. Markus A. Rüegg, und Dr. Iwona Ksiazek

Basel, den 23. Juni 2015

Prof. Jörg Schibler
Dekan

Contents

Summary

Col4a3 knock-out (Col4a3KO) mice, a genetic model of autosomal recessive Alport syndrome, are broadly used to study Alport disease and to test potential therapies. However, little is known about gender differences in the progression of renal disease in Col4a3KO mice although human autosomal form of Alport syndrome is shown to affect males and females equally. Furthermore, influx of macrophages is associated with disease progression in Alport kidney but their exact contribution remains elusive. In *chapter 1*, we investigated i) gender-phenotype correlations of Col4a3KO mice and ii) the role of macrophage in renal disease progression in Col4a3KO mice. We show that male and female Col4a3KO mice exhibit similar disease progression assessed by body weights, biomarkers of tubular injury, kidney function parameters and renal pathology. Those data demonstrate that Col4a3KO mice of both sexes can be used to study Alport disease and to evaluate experimental therapies. In addition, ~70% macrophage depletion in Col4a3KO kidney by clodronate liposome treatment did not improve renal pathology and kidney function. This result suggests that targeting macrophage alone is not sufficient to alleviate disease progression in Alport syndrome.

Dipeptidyl peptidase 9 (DPP9) is a cytosolic serine protease of unknown physiological function and substrates. *In vitro* studies suggest the role of DPP9 in cell behavior and immune response but there is no *in vivo* data supporting those findings. Recently, neonatal lethality of DPP9 enzyme inactive mice is reported but the cause of their death is unknown. In *chapter 2*, we investigated the cause of neonatal lethality of DPP9 enzyme inactive mice ($DPP9^{ki/ki}$ mice) and characterized their immune related phenotype to better understand the physiological role of DPP9 enzyme. We show that $DPP9^{ki/ki}$ mice die within 24 hours after birth due to the suckling defect as proven by their rescue by manual feeding. Maternal behavior, energy homeostasis, and development of sensory-motor neuronal pathways which can influence suckling response are normal in $DPP9^{ki/ki}$ mice. Instead, $DPP9^{ki/ki}$ mice display microglossia with defects in the formation of intrinsic distal tongue muscle which derive from migratory muscle progenitors. On the other hand, intrinsic proximal and extrinsic tongue muscles deriving from head mesenchyme formed normally in $DPP9^{ki/ki}$ mice. In accordance with defects in intrinsic distal tongue muscle, reduced number and

impaired survival of migratory tongue muscle progenitors are observed in $DPP9^{ki/ki}$ mice. CXCR4 signaling, known to be important for survival and migration of muscle progenitors, is not impaired in the absence of DPP9 enzymatic activity, although we cannot rule out that DPP9 enzyme regulates the function of SDF1, ligand of CXCR4. In addition, we show that $DPP9^{ki/ki}$ mice have defect in fetal hematopoiesis but their hematopoietic cells are fully functional and can reconstitute myeloid and lymphoid lineages in lethally irradiated mice. In summary, we report for the first time that DPP9 enzymatic activity controls survival of migratory tongue muscle progenitors. Absence of DPP9 activity results in impaired tongue development, suckling defect, and neonatal lethality in mice. However, DPP9 enzymatic activity in hematopoietic stem cells is not essential for normal hematopoiesis.

1

Contribution of gender and macrophages in Col4a3 knock-out mice

1.1 Introduction

Alport syndrome is an inherited genetic disease which affects approximately 1 in 5000 people and is caused by mutations in the type IV collagen genes (Hasstedt and Atkin 1983). In particular, mutations in the type IV collagen α5 chain gene (COL4A5) are responsible for the X-linked form of the disease, which accounts for ~85% of the patients and mutations in the type IV collagen α3 or α4 chain gene (COL4A3 or COL4A4) lead to the autosomal form of the Alport syndrome (Hertz et al. 2012). Type IV collagen assembles primarily as α3α4α5 heterotrimers in the adult glomerular basement membrane (GBM) and is one of the main structural components essential for GBM integrity and function. Mutations in any of the three collagen chains can result in defective assembly of the GBM leading to the renal pathology of Alport syndrome manifested by irregular thickening and splitting of the GBM, podocyte effacement, glomerulosclerosis with extracellular matrix deposition, kidney fibrosis, and ultimately, end stage renal disease (ESRD) early in life (Figure 1.1; Flinter 1997; Kruegel et al. 2013).

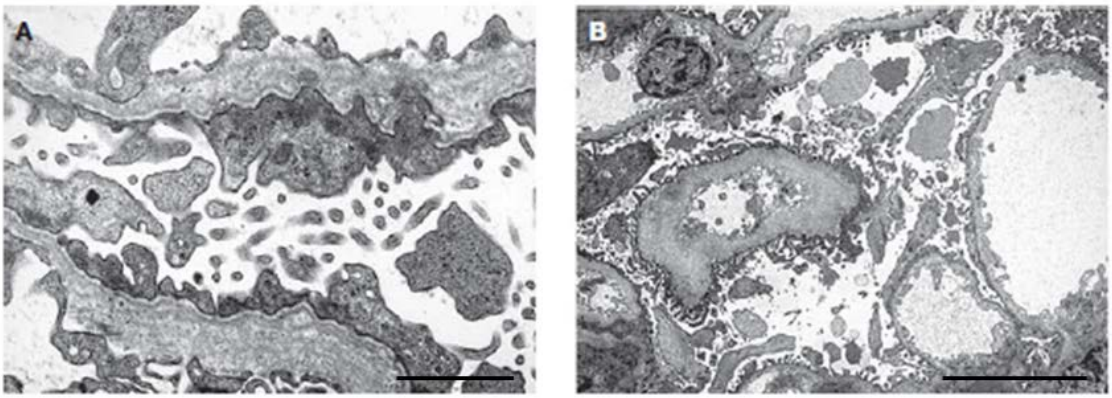

Figure 1.1 Electron microscopy images of renal tissue from patients with Alport syndrome. (**A**) Thickening and splitting of the GBM. Scale bar: 500 nm. (**B**) Irregular thickness of the GBM. Scale bar: 1 µm. (Gubler 2008)

Col4a3-deficient (Col4a3KO) mice are developed by gene targeting at the Col4A3 locus and are raised on a 129/SvJ genetic background. In the absence of type IV collagen α3, α4, and α5 chains, mice develop progressive glomerulonephritis as well as ESRD and die at an age of approximately 10 weeks (Cosgrove et al. 1996; Gross et al. 2003). The structural and functional manifestation of renal pathology of Col4a3KO mice closely resembles that of human Alport syndrome, making Col4a3KO mice an ideal model to understand Alport pathology. The translatability of Col4a3KO model for the autosomal recessive form of Alport syndrome is demonstrated by animal studies with Col4a3KO mice that have successfully assisted in identifying effective therapies for Alport patients. Well-established evidence comes from RAAS blockage with ACE inhibitors which delays progression to renal replacement therapies in humans with Alport syndrome (Gross et al. 2012; Temme et al. 2012) and is effective in delaying renal failure in Col4a3KO mice (Gross et al. 2003). While human autosomal form of Alport syndrome is shown to affect males and females equally (Mochizuki et al. 1994), relatively little is known about gender-specific susceptibility to disease progression in Col4a3KO mice. One of the goals of this study was to determine whether gender has a significant impact on the onset and progression of kidney disease in Col4a3KO mice.

It is well established that interstitial inflammation is a prominent feature of progressive renal diseases including Alport syndrome. As early as 1961, Whalen and colleagues reported the presence of CD68-positive foam cells in human Alport syndrome (Whalen et al. 1961). Foam cells belong to the monocyte-macrophage lineage and acquire their ‘foamy’ appearance owing to the accumulation of fat. Extensive macrophage infiltration is also reported for the Col4a3KO kidney with a strong correlation to the severity of kidney injury and fibrosis (Rodgers et al. 2003; Dennis et al. 2010). In spite of the association of macrophages with Alport syndrome, the contribution of macrophage infiltration to the progression of Alport syndrome remains elusive. Previous studies in Col4a3KO mice with agents attenuating monocyte-macrophage recruitment to kidney have yielded equivocal results, with one study showing improved renal pathology and mice survival (Ninichuk et al. 2005) and another showing no improvement (Clauss et al. 2009).

Clodronate is a transient, selective, and systemically acting macrophage-depleting agent (Van Rooijen and Sanders 1994; van Rooijen et al. 1996). The phagocytosis-mediated uptake of clodronate leads to suicidal apoptosis and abrogation of macrophage functions in the targeted organs. This depletion strategy has been successfully applied to ablate macrophages in other animal models of acute and chronic renal diseases (Jo et al. 2006; Kitamoto et al. 2009), but has not yet been reported in Alport syndrome mice.

This study was conducted to investigate i) the effect of macrophage depletion in the progression of Alport disease in Col4a3KO mice and ii) any gender-specific susceptibility of these mice to Alport disease. Animal weights, renal pathology, and renal biomarkers of function and injury were used to assess disease progression over time.

1.2 Results

Body weight in Col4a3KO mice of both genders

To study the progression of renal disease in male and female Col4a3KO (KO) mice, change in body weights are reported in comparison to wild-type (WT) littermates of the same sex. Up to the first 7 weeks of life, the weights of KO mice were largely indistinguishable from their respective WT littermates (Figure 1.2). After

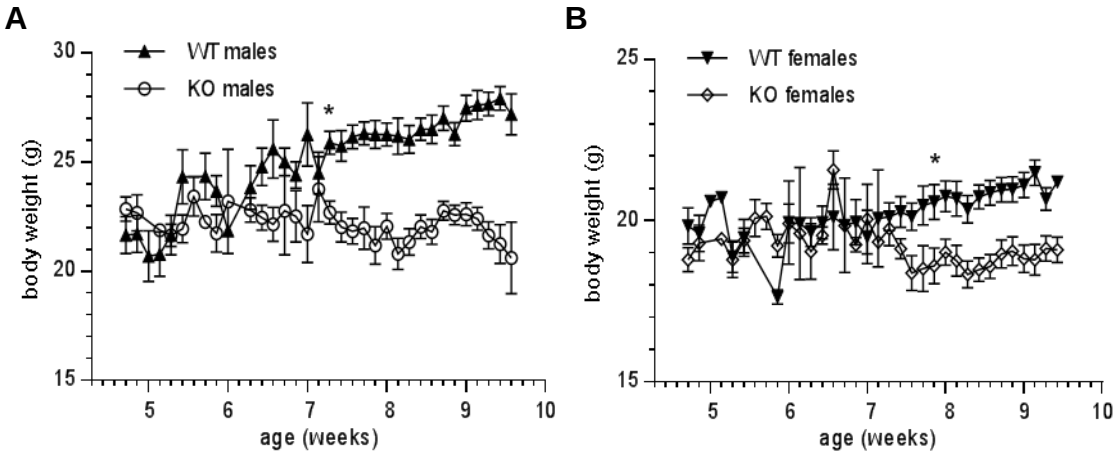

Figure 1.2. Body weights were reduced in male (**A**) and female (**B**) Col4a3KO mice as compared to WT littermates by 7.3 and 7.9 weeks of age, respectively (n=10 to 15 mice per group).

approximately 7 weeks of age, both male and female KO stopped gaining weight in contrast to their WT siblings, which continued to exhibit gradual increases in body weight. At the age of ~7.3 and 7.9 weeks (51 and 55 days), respectively, the male and female KO mice demonstrated significant lower body weights as compared to the age- and gender-matched WT siblings (12% and 10%, respectively). By 9 weeks of age, the male and female KO mice were lighter than age- and gender-matched WT by approximately 18% and 11%, respectively.

Change in renal function in Col4a3KO mice of both genders

To assess whether KO mice exhibit gender-dependent alterations in the onset and the kinetics of renal function decline, serum urea nitrogen (BUN) and urinary albumin were monitored weekly for both sexes from the age of 5 to 10 weeks. As shown in Figure 1.3A, serum BUN levels in 5-weeks old KO mice were comparable to the WT littermates with no discernable differences between the genders. However, by 6 weeks of age, both male and female KO displayed significantly elevated BUN levels as compared to their WT littermates (~2-fold). BUN levels gradually increased in both genders of KO mice until 8 weeks of age; at which time a ca. 7-fold increase in BUN was measured. By 10 weeks of age, BUN levels were on average 9- and 6-fold higher in KO males and females, respectively, compared to their WT littermates. Levels of BUN were comparable for female and male KO mice at all measured time points, except for weeks 9 and 10. Urinary albumin/creatinine ratios (henceforth referred to as albumin) were assessed in KO males and females between 5 to 10 weeks of age (Figure 1.3B). Albumin levels increased significantly in 5-week old KO mice with approximately 540- and 210-fold increases in males and females, respectively, compared to WT littermates. Albumin levels remained elevated over the entire observation period in KO, with ca. 580-fold and 1700-fold increases in males and females, respectively over WT level by 10 weeks of age. Levels of albumin were comparable for female and male KO mice at all measured time points, except for weeks 5 and 10.

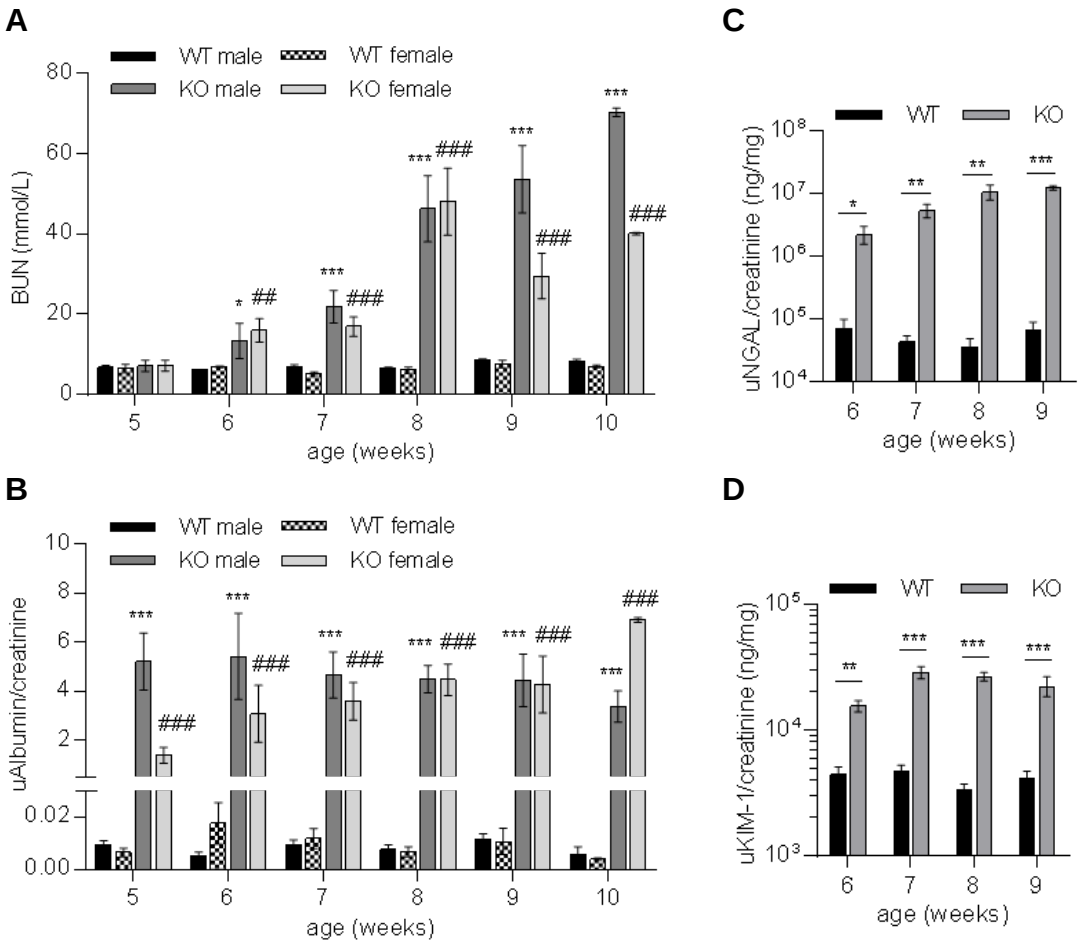

Figure 1.3. Increase in renal dysfunction biomarkers (**A, B**) accompanied an increase in kidney injury biomarkers (**C, D**) in Col4a3KO mice after 5 weeks of age. Serum BUN (**A**), urinary albumin (**B**), urinary NGAL (**C**), and urinary KIM-1 (**D**) levels were significantly increased in KO mice at 5-6 weeks of age and continued to increase until the end of the monitored period (10 weeks). *, significance vs WT males; #, significance vs WT females. (n=3 to 10 mice per group)

Change in kidney injury biomarkers in Col4a3KO mice

To investigate kidney injury, levels of neutrophil gelatinase-associated lipocalin (NGAL) and kidney injury molecule-1 (KIM-1) were systematically measured and normalized to urinary creatinine in KO mice from 6-10 weeks of age. NGAL and KIM-1 levels showed marked increases in the week 6 urine samples as compared to the age-matched WT mice and these continued to increase gradually throughout the study period (Figure 1.3C and D). Approximately 30- and 140-fold increases in NGAL were measured in 6-and 9-week old KO, respectively over the WT level. KIM-1 levels were increased 3- and 5-fold over WT in 6-and 9-week old KO, respectively. No gender differences in NGAL and KIM-1 levels were observed (data not shown).

Renal pathology in male and female Col4a3KO mice

Pathological examination of kidney tissue from 8 weeks old mice confirmed the most prominent histopathological features of Alport syndrome in both female and male KO mice (Figure 1.4). Histological examination of hematoxylin/eosin (H&E) (Figure 1.4A-C) and periodic acid-Schiff (PAS) (not shown) sections showed multifocal to diffused processes affecting the cortex and the medullary regions of the kidney. Many of the dilated tubules either contained eosinophilic material (casts) or showed degeneration/atrophy with short basophilic to coarsely vacuolated epithelial cells. Generalized involvement of the glomeruli by variable thickening of the basement membrane or segmental to diffused obscuration of the glomerular structure (glomerular sclerosis) was also observed. The interstitium was multifocally thickened by few cells resembling fibroblasts and more rarely, inflammatory cells. H&E or PAS showed increased deposition of collagen at the corticomedullary junction or in the vicinity of sclerotic glomeruli. Sirius red stain showed diffused and exaggerated deposition of extracellular matrix (ECM) (Figure 1.4D-F). Both genders were affected equally by disease progression as indicated by nephropathy score and assessment of interstitial fibrosis (Figure 1.4E).

F4/80 and α-smooth muscle actin (α-SMA) staining showed occurrence of fibrotic lesions characterized by infiltrates of F4/80 positive macrophages and α-SMA-positive myofibroblasts in KO mice of both genders (data not shown). Morphometric quantification confirmed a significant increase in macrophage and myofibroblast infiltrates in the KO kidney (Figure 1.5A). Male and female kidneys were similarly affected with 12-fold and 36-fold increases respectively, in F4/80 and 12- and 13-fold increases respectively, in α-SMA staining as compared to age-matched WT mice. To correlate protein data with transcriptional expression the mRNA expression of Col3A1, F4/80 and Thy-1 genes were investigated by real-time PCR (Figure 1.5B). Previous studies have shown Col3A1 and Thy-1 (CD90) transcripts to be highly elevated in KO kidney (Sampson et al. 2001). Thy-1 has also been described to co-localize with α-SMA-positive myofibroblasts in several organs, including kidney, and represents a useful expression marker for myofibroblasts (Clayton et al. 1997; Dudas et al. 2007). In agreement with previous studies, significant changes in Col3A1, F4/80 and Thy-1 gene expression are reported here, with 44-, 9-, and 18-fold increases in KO

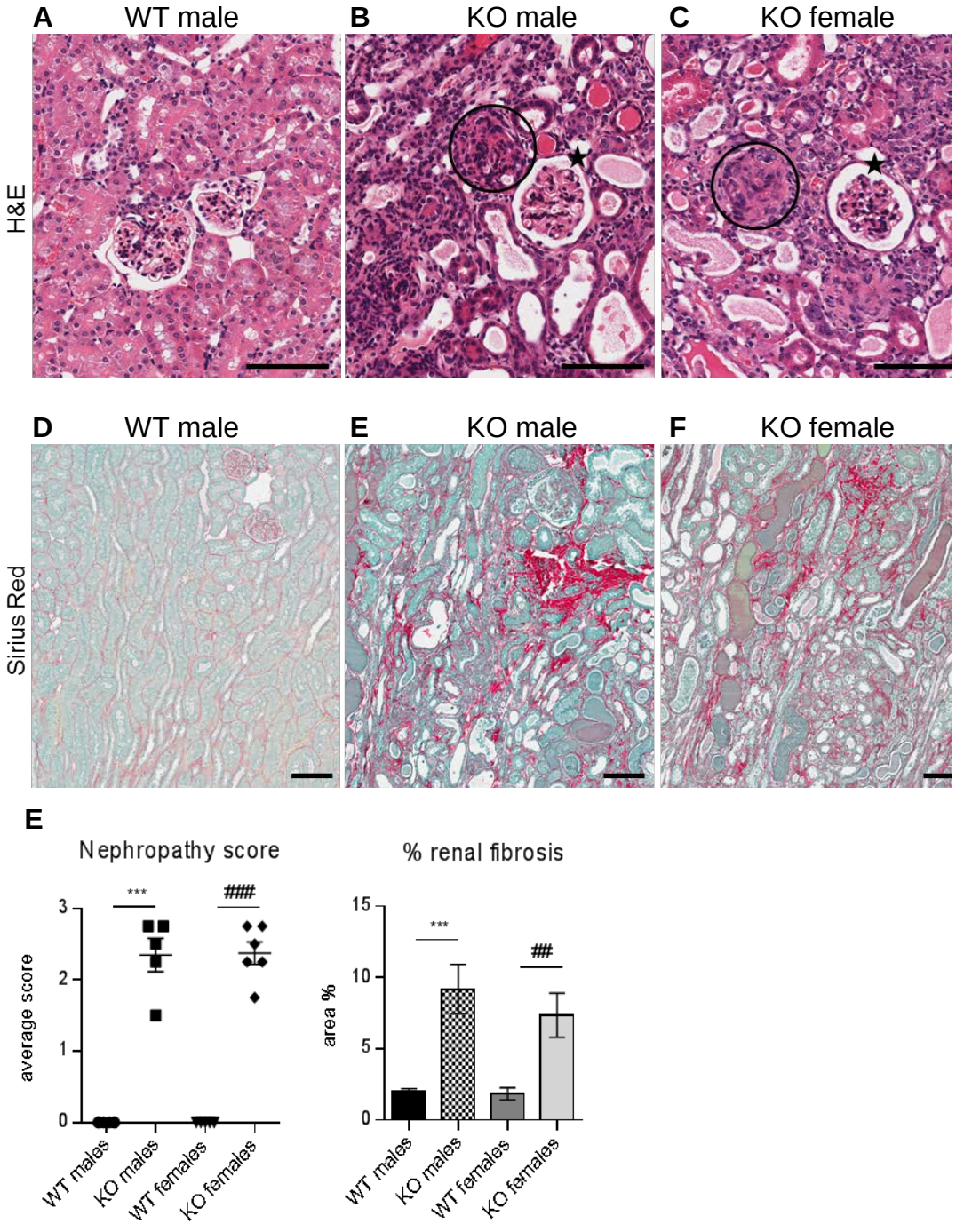

Figure 1.4. No differences in renal pathology noted between male and female Col4a3KO kidney at 8 weeks of age. (**A-C**) H&E-stained cortex. KO mice showed glomerulosclerosis (circled) to varying degrees, with some glomeruli appearing less affected and almost normal (stars). (**D-F**) Sirius red-stained cortex. WT showed a thin delineation of Sirius Red-stained fibers around tubuli, in KO this was variably thickened.. (**E**) Nephropathy score assessed in H&E- and PAS-stained sections and quantitative analysis of Sirius Red positive interstitial fibrosis demonstrated significantly increased nephropathy and interstitial fibrosis in KO mice compared to WT littermate controls of the same sex with no differences between female and male mice. Scale bar 100 µm.

male kidney relative to wild-type mice and similar extent of increases observed in KO females. The gene expression and protein composition data are consistent with the histopathological changes with no discernable differences in disease onset or progression between female and males KO mice. This observation and the absence of gender-associated weight differences with disease progression justified the use of only male mice henceforth in this study.

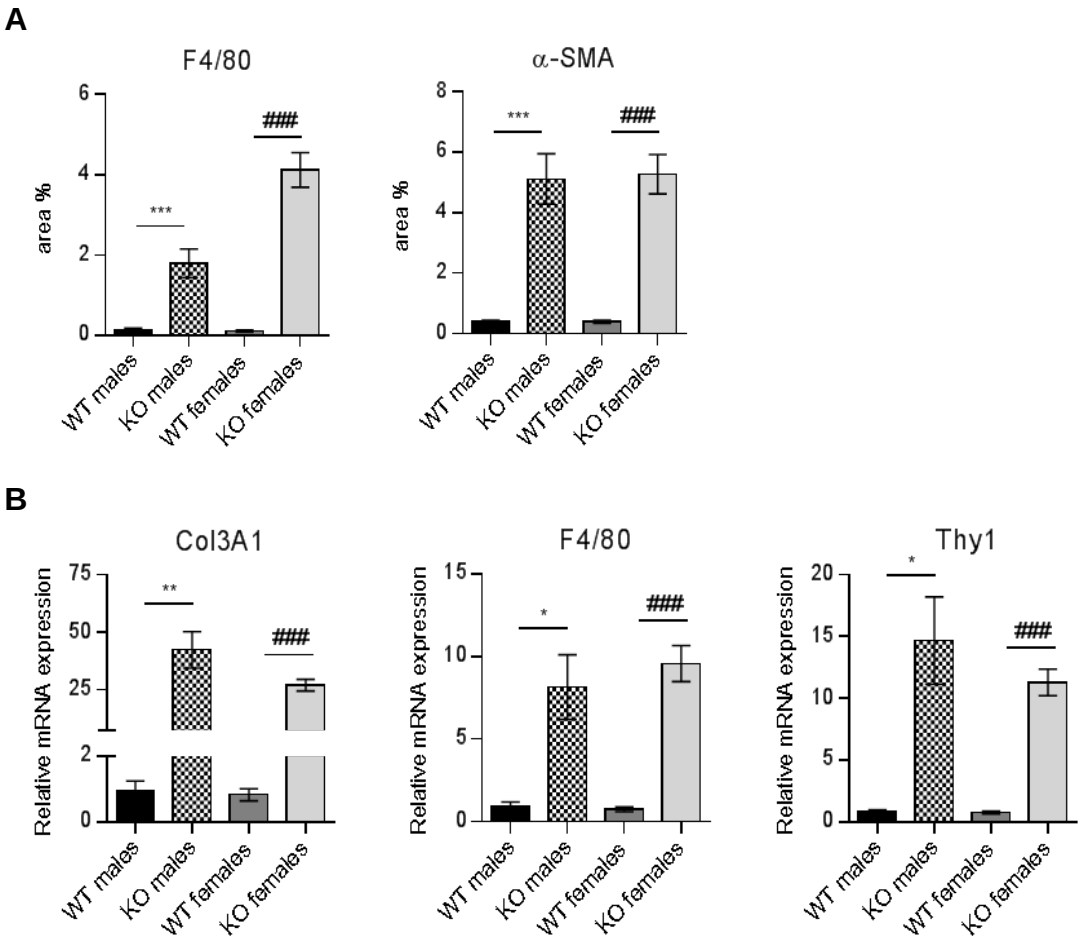

Figure 1.5. Protein and mRNA expression of collagen, macrophages, and myofibroblasts markers were increased in 8 weeks old Col4a3KO mice with no significant differences between male and female mice. (**A**) Morphometric analysis of F4/80-positive macrophages and α-SMA-positive myofibroblasts showed a significant increase was observed in both male and female KO kidney, compared to WT littermate controls of the same sex. The degree of changes was comparable in animals of both genders with the exception of the F4/80 positive macrophage area being about two-fold higher in female than in male KO mice. (**B**) Real-time PCR analysis of Col3A1, F4/80 and Thy-1 mRNA showed marked upregulation in the expression of these genes in both male and female KO kidney, compared to WT littermate controls of the same sex. The magnitude of changes was comparable in animals of both genders. *: significance vs WT males; #: significance vs WT females. n=3 to 8 mice per group.

Effect of macrophage-depletion on kidney function and fibrosis

To investigate the contribution of macrophages to Alport disease, kidney macrophages were depleted in Col4a3KO mice using clodronate liposomes (KO+CL) and compared to PBS liposome-treated mice (KO+PBSL), untreated Col4a3KO (KO), and wild-type (WT) littermate mice (Figure 1.6A). Treatment with CL and PBSL was initiated in 4-weeks old mice since disease onset measured by proteinuria was not observed until 5 weeks of age (Cosgrove et al. 1996). Diffused infiltration of F4/80 macrophages in KO+PBSL kidneys was effectively inhibited through the administration of CL (Figure 1.6B). After 4 weeks of treatment with KO+CL, 70% macrophage depletion was observed as demonstrated by protein and gene expression analyses (Figure 1.6C and D).

The effect of macrophage depletion on the onset and severity of Alport disease was studied in Col4a3KO mice by assessing renal function and interstitial fibrosis. KO+CL mice progressed to renal failure with similar degree and severity as KO+PBSL or KO mice (Figure 1.7). Kidney function was not improved as indicated by comparable levels of serum BUN and urine albumin, between the KO+CL and KO+PBSL mice within the 4-8 week time span (Figure 1.7A and B). A transient change in urinary albumin was measured only in 7-weeks old KO+PBSL mice and could account for significantly lower levels in KO+CL mice. No effect of macrophage depletion on the levels of NGAL and KIM-1 were observed in 8-week old mice (Figure 1.7C and D). Histological analyses did not reveal any differences in renal pathology, with all KO mice showing a similar extent in the severity and distribution of chronic renal pathology, regardless of the treatment received (Figure 1.8 and 9). The overall nephropathy score was not remarkably different following macrophage depletion (Figure 1.8E). A minimal decrease in glomerular sclerosis was observed in KO+CL mice when compared to KO mice, however there was no reduction when compared with the KO+PBSL mice (Figure 1.8E). Similarly, no reduction in α-SMA-positive cells was observed in KO+CL mice when compared to KO+PBSL mice (Figure 1.9C-E). The elevated expression of profibrotic genes (Figure 1.9F) as wells as genes of ECM remodeling (Figure 1.9G) and inflammation (Figure 1.9H) did not differ in KO mice from different treatment groups.

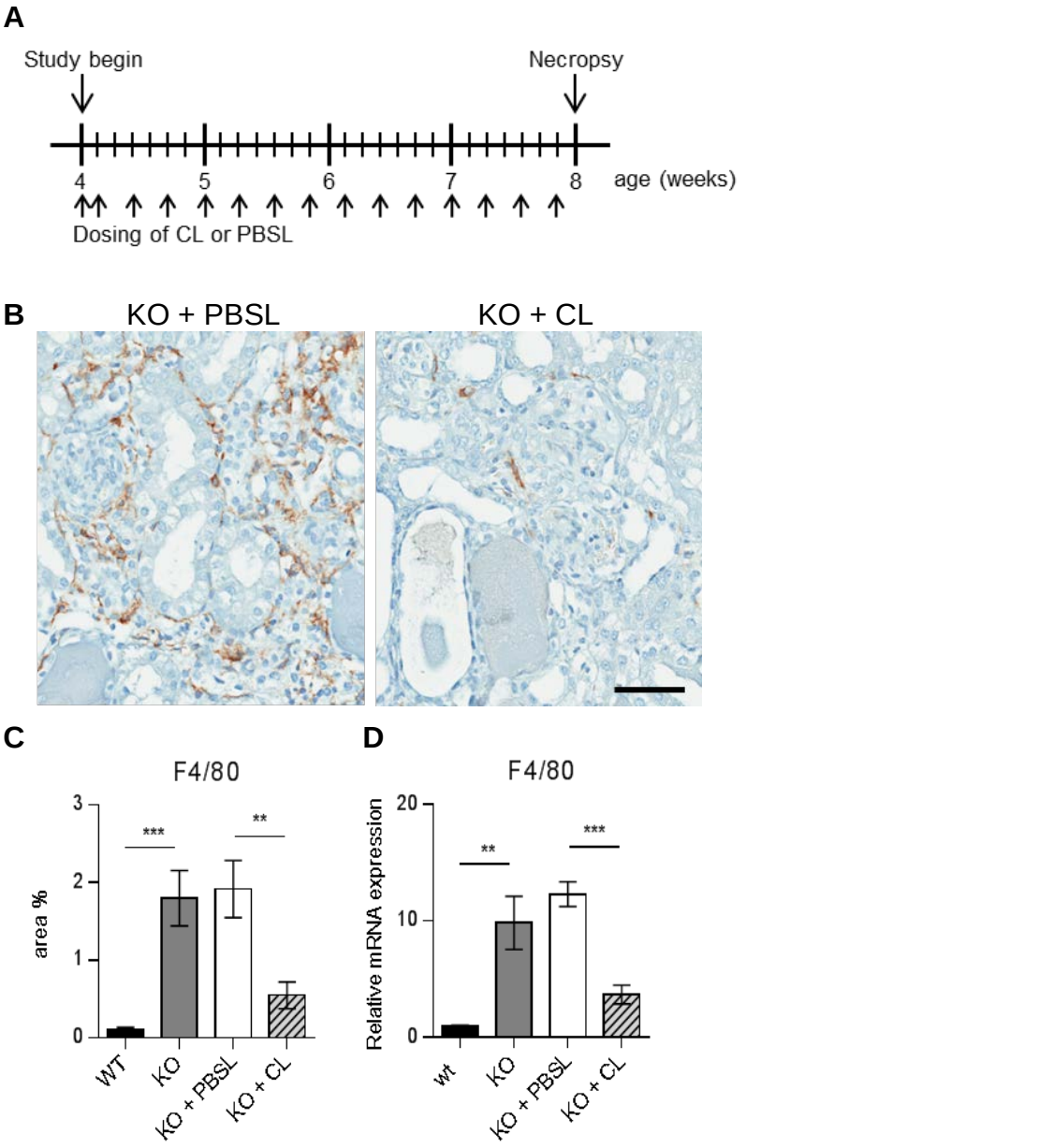

Figure 1.6. Clodronate liposome mediated macrophage depletion in Col4a3KO mice. (**A**) Col4a3KO male mice were dosed intraperitonally with CL (KO+CL) or PBSL (KO+PBSL) as control. Animals were entered in the study at the age of 4 weeks and were continually dosed until the age of 8 weeks. Injections were repeated every second day, except for the first two doses, which were injected on consecutive days. (**B-D**) CL significantly reduced F4/80 positive macrophage infiltrates in KO kidneys at the age of 8 weeks. (**B, C**) Representative images and quantitative assessment of F4/80 stained macrophages in kidney sections revealed marked reduction in macrophage infiltrates following CL dosing in KO mice. (**D**) Real-time PCR analysis of F4/80 mRNA expression in KO+CL, KO+PBSL, KO, and WT littermates at the age of 8 weeks. Significant reduction in F4/80 mRNA expression following CL dosing was observed. Scale bar: 100 µm. n=5 mice per group. CL: clodronate liposomes; PBSL: PBS liposomes.

Although monocytes-macrophages are reported to be one of the cell types expressing TGF-β1 in the mouse Alport kidney (Rodgers et al. 2003), reduction of macrophages by 70% did not affect TGF-β1 expression, which appear to be increased 4-fold in KO mice as shown in this study (Figure 1.9F) as well as in other studies (Sampson et al. 2001). This indicates that macrophages are likely not the major cellular source of TGF-β1 in the Col4a3KO kidney.

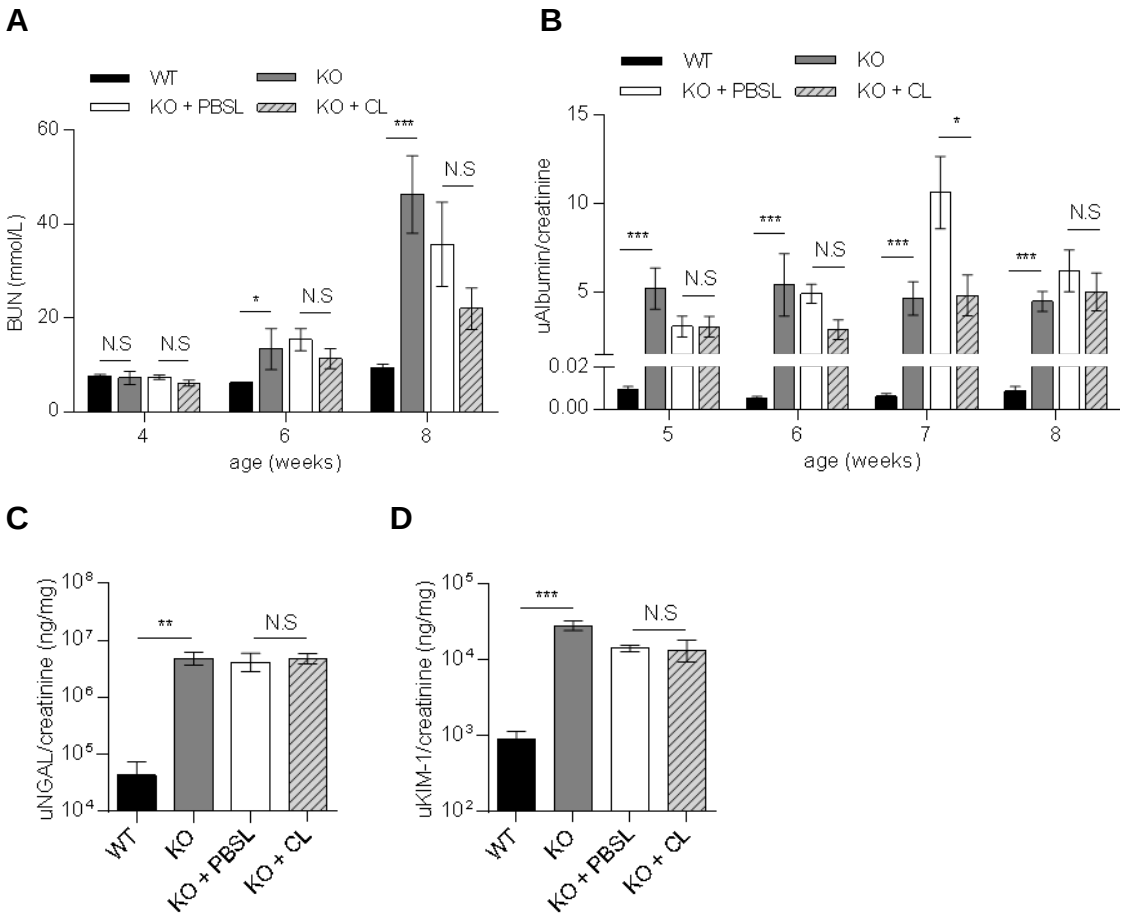

Figure 1.7. Macrophage depletion did not improve renal function in Col4a3KO mice. (**A-D**) CL treatment did not delay or slow down renal failure measured by serum BUN and urinary albumin, NGAL, and KIM-1. (**A, B**) Similar increase in BUN and ACR was detected at all time points in KO+CL compared to KO+PBSL or KO mice. (**C, D**) KO+CL mice showed similar increase in urinary NGAL and KIM-1 as KO+PBSL or KO mice at the age of 8 weeks. n=5 to 9 mice per group. CL: clodronate liposomes; PBSL: PBS liposomes.

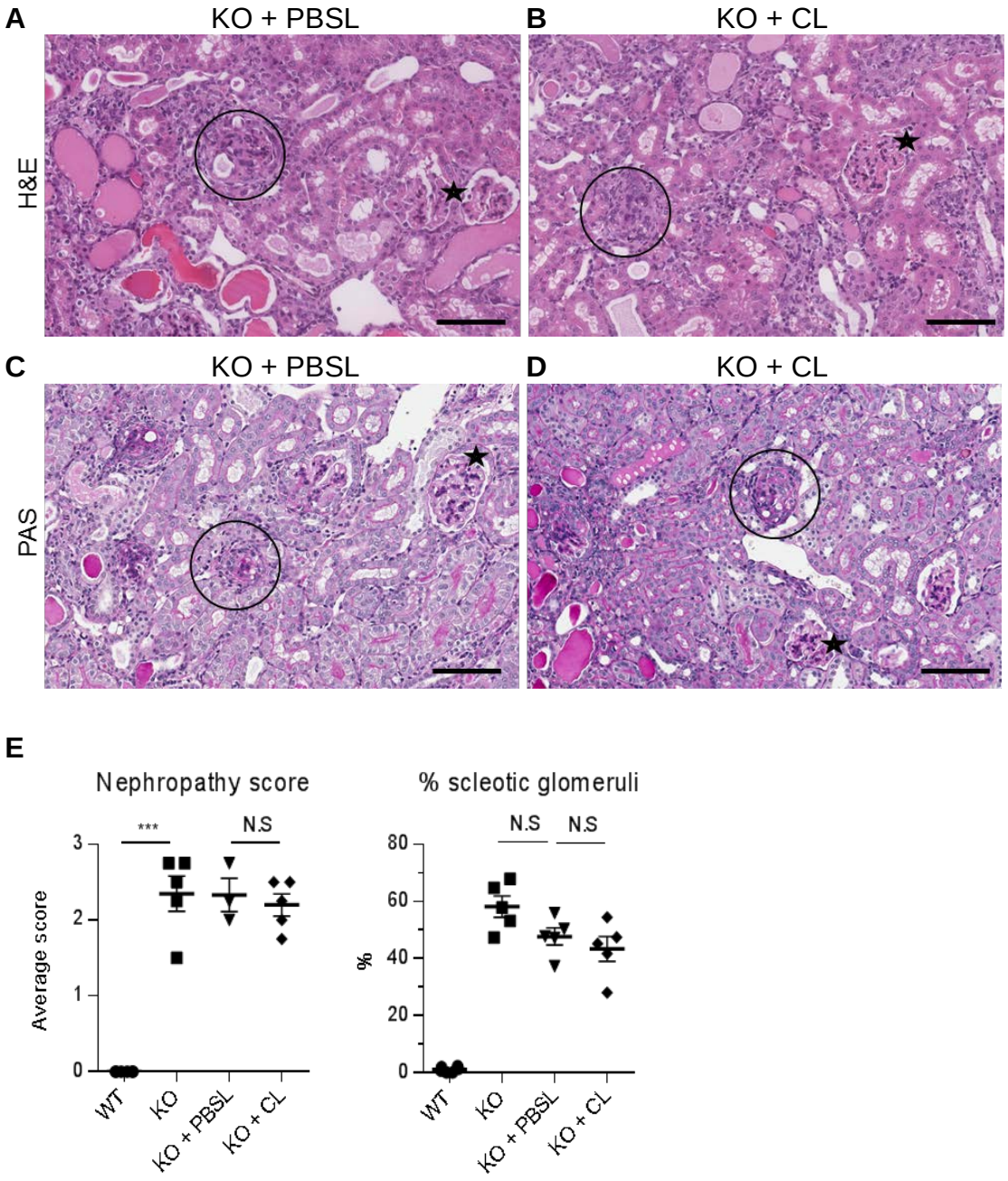

Figure 1.8. Macrophage depletion did not improve renal pathology in Col4a3KO mice. Kidney pathology was comparable between KO+PBSL and KO+CL. Panels **A** (H&E) and **C** (PAS) show tubular pathology (atrophy, degeneration/regeneration and eosinophilic casts) in KO+PBSL; panels **B** (H&E) and **D** (PAS) show comparable tubular pathology in KO+CL. Incidence of sclerotic glomeruli was comparable between KO+PBSL and KO+CL (circle = sclerotic glomeruli; star = normal-appearing glomeruli), with many glomeruli showing variable extent of changes from normal to sclerotic appearance. (**E**) Semi quantitative histologic assessment of nephropathy and sclerotic glomeruli revealed no significant differences between KO, KO+PBSL or KO+CL mice. Scale bar 100 µm. CL: clodronate liposomes; PBSL: PBS liposomes.

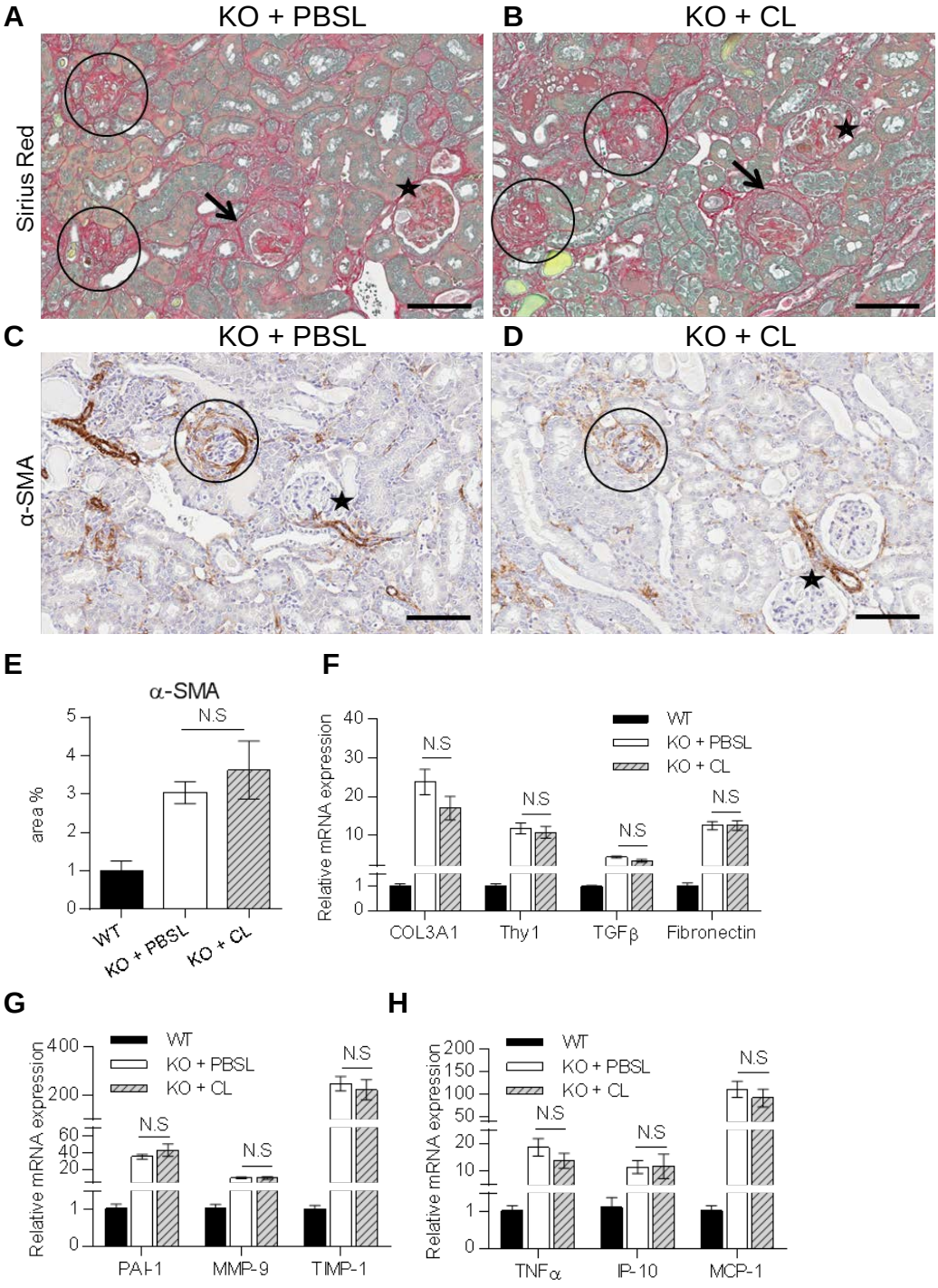

Figure 1.9. Macrophage depletion showed no effect on interstitial fibrosis and myofibroblast accumulation in Col4a3KO mice. A (Sirius red) and **C** (α-SMA) show increased deposition of Sirius red stained fibrotic tissue and α-SMA cells in the interstitium of KO+PBSL; **B** (Sirius red) and **D** (α-SMA) show an increased staining of the interstitium in KO+CL that was comparable to KO+PBSL (circle: sclerotic glomeruli; star: normal-appearing glomeruli). Glomerular crescents (arrows) were also observed occasionally in glomeruli. (**E**) Morphometric analysis of α-SMA stained myofibroblasts confirmed no discernable effect of CL treatment on myofibroblasts deposition. (**F-H**) Expression of profibrotic genes (**F**), genes for ECM remodeling (**G**) and inflammation (**H**) is comparable in KO+PBSL and KO+CL mice. Scale bar 100 µm. CL: clodronate liposomes; PBSL: PBS liposomes.

1.3 Discussion

Gender-independent progression of kidney disease in Col4a3KO mice.

The human autosomal form of Alport syndrome has been shown to affect both males and females equally (Mochizuki et al. 1994). However, little is known about gender differences in renal disease progression in Col4a3KO mice. This study demonstrates that the severity of disease onset and progression is not dependent upon gender of Col4a3KO mice. Thus, both female and male Col4a3KO mice are equally predictive of Alport syndrome and can be used to study pathogenic mechanisms and to evaluate experimental therapies.

NGAL and KIM-1 are produced by kidney in response to tubular epithelial damage (Ichimura et al. 1998; Mishra et al. 2003). Urinary NGAL and KIM-1 were systematically evaluated in Col4a3KO mice as markers of kidney injury along with BUN and urinary albumin, the standard measures of renal function. NGAL and KIM-1 were markedly elevated during early to late stage disease progression in Col4a3KO mice, supporting their role as markers of kidney damage. A similar pattern of increased NGAL excretion was also found in dogs with the X-linked form of Alport syndrome (Nabity et al. 2012) suggesting a conserved pattern of NGAL expression in Alport nephropathy across multiple species. Further investigation would need to confirm the use of NGAL and KIM-1 as translational biomarkers of human autosomal recessive Alport disease.

Macrophages depletion does not alleviate disease progression in kidney of Alport mice.

To test the hypothesis that macrophage depletion would improve kidney function and renal pathology in Alport disease, Col4a3KO male mice were treated with CL. CL treatment, started prior to onset of disease as evidenced by clinical pathology and continued throughout the study, effectively reduced macrophage recruitment to the Alport kidney by ~70%. However, the reduction of macrophages was not associated with improvement of histological or functional renal injury in Col4a3KO mice.

These data are in agreement with a previous study, which showed that significant inhibition of macrophage infiltration alone (via MCP-1/CCL2 blockage using anti-CCL2 spiegelmers) led to the reduction of glomerular and interstitial macrophages by

50% and 30%, respectively, but was not associated with improving renal pathology or prolonging the life span of Col4a3KO mice (Clauss et al. 2009). Although 70% macrophage depletion was achieved in the current study, any compensatory role by the remaining 30% macrophages in driving renal damage in Col4a3KO mice cannot be eliminated. Macrophage populations are not all the same, as shown by *in vitro* studies that differentiate between two major populations; M1 and M2, according to their response to specific cytokines. Both renoprotective and damaging effects have been attributed to M2 macrophages. Adoptive transfer of M2 macrophages has been shown to resolve inflammation and repair injury in many fibrosis models of kidney injury (Wang and Harris 2011). Similarly the ablation of macrophages during the M2 predominance is shown to slow kidney resolution in the reperfusion injury model (Lee et al. 2011). On the contrary, conditional ablation of M2 macrophages defined as $Ly6C^{low}$ has been shown to be antifibrotic in unilateral ureteral obstruction (UUO) model of kidney fibrosis (Lin et al. 2009). Clodronate treatment can kill activated M2 macrophages (Wu et al. 2014) but the extent to which specific macrophage sub-populations are affected by clodronate or the contribution of these subpopulations in Alport syndrome has not been investigated in this or previous studies. The extent of macrophage depletion in kidney obtained in Col4a3KO mice was similar to that obtained in UUO where CL-mediated macrophage depletion prior to the UUO injury resulted in the amelioration of renal fibrosis (Kitamoto et al. 2009).

Partial depletion (25%) of interstitial macrophages via the antagonism of chemokine (C-C motif) receptor 1 (CCR1), associated with a reduction of transendothelial migration of blood leukocytes, is reported to have a moderate effect on renal function as well as survival of Col4a3KO mice (Ninichuk et al. 2005). The results from our study indicate that macrophage depletion by clodronate treatment neither ameliorated, nor potentiated fibrosis in Col4a3KO mice. A possible explanation for the varied results regarding the impact of macrophage depletion in the progression of Alport disease is that a broad spectrum of leukocytes and not exclusively the monocyte/macrophage population are important for disease progression. In agreement with this, interstitial T-cell infiltrates are observed in renal biopsies of patients with Alport syndrome and are shown to inversely correlate with renal function of patients with Alport syndrome (Jedlicka et al. 2010). This hypothesis is also supported by

observations from previous studies, in which Col4a3KO mice either crossed with RAG-1 deficient mice to lack mature lymphocytes or treated with a statin inhibitor to reduce both lymphocytes and macrophages alleviated Alport kidney pathology and prolonged survival. Specifically, Col4a3KO mice crossed with RAG-1-deficient mice showed reduced tubulointerstitial inflammation and fibrosis without improving the glomerular injury (Lebleu et al. 2008), while treatment with a statin inhibitor, had antifibrotic effect and prolonged the survival of Col4a3KO mice (Koepke et al. 2007). The data presented here strongly suggest that inhibition of macrophage infiltration alone is not sufficient to ameliorate progression of Alport syndrome in Col4a3KO mice and collectively with data from other studies (Kruegel et al. 2013; Gross et al. 2014) suggest that, targeting multiple immune cell populations will likely be more effective in checking kidney disease progression.

1.4 Conclusions

Alport syndrome is a genetic disease of collagen IV (α3, 4, 5) resulting in defective assembly of glomerular basement membrane leads to renal failure. Col4a3KO mice are an established genetic model of autosomal recessive Alport syndrome. No sex differences in the evolution of body mass loss, renal pathology, biomarkers of tubular damage NGAL and KIM-1, or deterioration of kidney function were observed during the life span of Col4a3KO mice. These findings confirm that, similar to human autosomal recessive Alport syndrome, female and male Col4a3KO mice develop renal failure at the same age and with similar severity. The specific contribution of macrophage infiltration to Alport disease, one of the prominent features of the disease in human and Col4a3KO mice, remains unknown. This study shows that depletion of kidney macrophages in Col4a3KO male mice by administration of clodronate liposomes, prior to clinical onset of disease and throughout the study period, does not protect the mice from renal failure and interstitial fibrosis, nor delay disease progression. These results suggest that therapy targeting macrophage recruitment to kidney is unlikely to be effective as treatment of Alport syndrome.

1.5 Materials and methods

Mice

Col4a3KO mice with 129/SvJ background (129-Col4a3^{tm1Dec}/J) were purchased from The Jackson Laboratory and maintained as a heterozygous colony. All animal studies were approved by the animal care committee of the Canton Basel-Stadt, Switzerland.

Animal studies

The gender and genotype of Col4a3KO mice was determined at 3 to 4 weeks of age. Both genders of Col4a3KO mice and their wild-type littermate controls of the same sex were used for the experiments unless stated differently. To analyze the gender effect, the study was initiated in 4 weeks old mice and terminated when the mice reached the age of 9-10 weeks or lost more than 20% of their body weight. The study with clodronate liposomes (CL) or PBS liposomes (PBSL) (Encapsula NanoSciences) was initiated in 4 week old mice and terminated when the mice reached the age of 8 weeks. Liposomes (200 µl/mouse) were injected intraperitoneally for 2 consecutive days, followed by every second day of administration until end of the study.

Urine and blood analysis

Urine was sampled weekly and analyzed for albumin, creatinine, NGAL, and KIM-1. Albumin was measured using the Albuwell M kit (Exocell) and normalized to creatinine levels analyzed by Aution urine analysis system (Arkray).
Mouse KIM-1 was analyzed with an immunoassay using an anti-mouse rat monoclonal and an anti-mouse goat polyclonal as the capture and detection reagent, respectively (R&D Systems) on an SI6000 from Mesoscale Discovery (MSD). 30 µL of capture antibody (4 µg/ml in PBS) was incubated overnight on MSD standard plates at 4°C. The plate was washed 3× with PBS followed by the addition of 25 µl of urine (1:4 dilution in MSD diluent 5) and incubated for 1 h at RT. Incubation with the secondary antibody for 1 h was followed by a wash and application of MSD Sulfo-Tagged anti-goat antibody for 1 h. After another wash, 150 µl of MSD Read Buffer T was added, and the plates read on an MSD SI 6000. Data were analyzed on MSD Discovery Workbench software. NGAL and Albumin were assayed at 1:1000 and 1:100 dilutions, respectively as per manufacturer's instruction using kits from Bioporto and Abnova, respectively. KIM-1 and NGAL were normalized to creatinine analyzed using the

Urinary Detection Kit (Arbor Assays) at a 1:25 dilution in H_2O and assayed as per manufacturer's instructions. Plates were read on a SpectraMax M5 (Molecular Devices) and analyzed with SoftMax Pro v5 (Molecular Devices).
Blood was sampled every two weeks from V. sublingualis into Microtainer tubes (BD biosciences) under isoflurane anesthesia. Serum was used to measure blood urea nitrogen by Spotchem EZ Automated analyzer and Spotchem ll reagent strip (Arkray).

Immunohistochemistry and histology

Kidneys were fixed in 10% buffered formalin for 48 h at RT and processed for embedding in paraffin using standard procedures. Immunohistochemical staining for F4/80 was performed using an automated Ventana Discovery XT Platform (Ventana medical systems). Sections, pretreated with protease (Ventana), were incubated with Peroxidazed 1 (Biocare medical) and stained with anti-F4/80 antibodies (1:100; ABD Serotec) for 48 min. Reaction was detected with the OmniMap anti-Rt HRP (Ventana) and ChromoMap DAB Kit (Ventana), followed by counterstaining with hematoxylin. For α-SMA staining, sections were treated with 0.5% H_2O_2 in methanol for 20 min, followed by 20 min incubation with anti-α-SMA antibodies (1:25; DAKO), detection by ARK™ Peroxidase kit (DAKO), and counterstaining with hematoxylin. For Sirius red staining, Picrosirius Red solution and 0.04% Light Green solution (EMS) were used according to the manufacturer's recommendations. Sections were stained with hematoxylin and eosin (H&E) and Periodic acid-Schiff (PAS) using standard protocols. Digital images were obtained with a ScanScope XT system (Leica).

Quantification of immunohistochemical staining

Area %, defined as stained area per total surface area, was obtained with Image Scope software (Leica) using the Positive Pixel Count algorithm.

Histopathological evaluation

Glomerular sclerosis percentages were assessed by counting the number of segmental to global sclerotic glomeruli, and other glomeruli with variable changes but with patent vessels on H&E sections. Tubulointerstitial change indices were obtained from H&E slides as the mean value between the semiquantitive score assigned to each change (namely tubular degeneration/atrophy, tubular dilation, tubular casts, and interstitial

fibrosis, with four-grade score system related to the extent of the change: 0, no lesion; 1, < 25% affected tubuli; 2, 25 to 50 % affected tubuli; 3, 51 to 75% of affected tubuli; 4, > 75% affected tubuli).

Real time qRT-PCR analysis

Kidney tissue was snap frozen in liquid nitrogen and homogenized with the FastPrep-24 (MP Biomedicals) system. RNA was isolated using an RNeasy purification kit (Qiagen) according to the manufacturer's recommendations. Quantitative real-time PCR was performed for genes of interest and 18s rRNA using Taqman Universal Master Mix and the ABI Prism 7900 HT Sequence Detection System (Applied Biosystems). Gene expression was normalized to 18s rRNA expression.

Statistical analysis

The results are presented as mean ± SEM. Unpaired t test was used for the comparisons between two groups. * or #: $p< 0.05$; ** or ##: $p <0.01$; *** or ###: $p <0.001$. For repeated measurements, data were analyzed using mixed model data analysis followed by posthoc Fisher's LSD test.

1.6 References

Clauss S, Gross O, Kulkarni O, Avila-Ferrufino A, Radomska E, Segerer S, Eulberg D, Klussmann S, Anders HJ. 2009. Ccl2/Mcp-1 blockade reduces glomerular and interstitial macrophages but does not ameliorate renal pathology in collagen4A3-deficient mice with autosomal recessive Alport nephropathy. *The Journal of pathology* **218**: 40-47.

Clayton A, Steadman R, Williams JD. 1997. Cells isolated from the human cortical interstitium resemble myofibroblasts and bind neutrophils in an ICAM-1--dependent manner. *Journal of the American Society of Nephrology : JASN* **8**: 604-615.

Cosgrove D, Meehan DT, Grunkemeyer JA, Kornak JM, Sayers R, Hunter WJ, Samuelson GC. 1996. Collagen COL4A3 knockout: a mouse model for autosomal Alport syndrome. *Genes & development* **10**: 2981-2992.

Dennis J, Meehan DT, Delimont D, Zallocchi M, Perry GA, O'Brien S, Tu H, Pihlajaniemi T, Cosgrove D. 2010. Collagen XIII induced in vascular endothelium mediates alpha1beta1 integrin-dependent transmigration of monocytes in renal fibrosis. *Am J Pathol* **177**: 2527-2540.

Dudas J, Mansuroglu T, Batusic D, Saile B, Ramadori G. 2007. Thy-1 is an in vivo and in vitro marker of liver myofibroblasts. *Cell and tissue research* **329**: 503-514.

Flinter F. 1997. Alport's syndrome. *J Med Genet* **34**: 326-330.

Gross O, Beirowski B, Koepke ML, Kuck J, Reiner M, Addicks K, Smyth N, Schulze-Lohoff E, Weber M. 2003. Preemptive ramipril therapy delays renal failure and reduces renal fibrosis in COL4A3-knockout mice with Alport syndrome. *Kidney international* **63**: 438-446.

Gross O, Licht C, Anders HJ, Hoppe B, Beck B, Tonshoff B, Hocker B, Wygoda S, Ehrich JH, Pape L et al. 2012. Early angiotensin-converting enzyme inhibition in Alport syndrome delays renal failure and improves life expectancy. *Kidney international* **81**: 494-501.

Gross O, Perin L, Deltas C. 2014. Alport syndrome from bench to bedside: the potential of current treatment beyond RAAS blockade and the horizon of future therapies. *Nephrology, dialysis, transplantation : official publication of the European Dialysis and Transplant Association - European Renal Association* **29 Suppl 4**: iv124-130.

Gubler MC. 2008. Inherited diseases of the glomerular basement membrane. *Nature clinical practice Nephrology* **4**: 24-37.

Hasstedt SJ, Atkin CL. 1983. X-linked inheritance of Alport syndrome: family P revisited. *American journal of human genetics* **35**: 1241-1251.

Hertz JM, Thomassen M, Storey H, Flinter F. 2012. Clinical utility gene card for: Alport syndrome. *European journal of human genetics : EJHG* **20**.

Ichimura T, Bonventre JV, Bailly V, Wei H, Hession CA, Cate RL, Sanicola M. 1998. Kidney injury molecule-1 (KIM-1), a putative epithelial cell adhesion molecule containing a novel immunoglobulin domain, is up-regulated in renal cells after injury. *The Journal of biological chemistry* **273**: 4135-4142.

Jedlicka J, Soleiman A, Draganovici D, Mandelbaum J, Ziegler U, Regele H, Wuthrich RP, Gross O, Anders HJ, Segerer S. 2010. Interstitial inflammation in Alport syndrome. *Human pathology* **41**: 582-593.

Jo SK, Sung SA, Cho WY, Go KJ, Kim HK. 2006. Macrophages contribute to the initiation of ischaemic acute renal failure in rats. *Nephrology, dialysis, transplantation : official publication of the European Dialysis and Transplant Association - European Renal Association* **21**: 1231-1239.

Kitamoto K, Machida Y, Uchida J, Izumi Y, Shiota M, Nakao T, Iwao H, Yukimura T, Nakatani T, Miura K. 2009. Effects of Liposome Clodronate on Renal Leukocyte Populations and Renal Fibrosis in Murine Obstructive Nephropathy. *Journal of Pharmacological Sciences* **111**: 285-292.

Koepke ML, Weber M, Schulze-Lohoff E, Beirowski B, Segerer S, Gross O. 2007. Nephroprotective effect of the HMG-CoA-reductase inhibitor cerivastatin in a mouse model of progressive renal fibrosis in Alport syndrome. *Nephrology, dialysis, transplantation : official publication of the European Dialysis and Transplant Association - European Renal Association* **22**: 1062-1069.

Kruegel J, Rubel D, Gross O. 2013. Alport syndrome--insights from basic and clinical research. *Nature reviews Nephrology* **9**: 170-178.

Lebleu VS, Sugimoto H, Miller CA, Gattone VH, 2nd, Kalluri R. 2008. Lymphocytes are dispensable for glomerulonephritis but required for renal interstitial fibrosis in matrix defect-induced Alport renal disease. *Laboratory investigation; a journal of technical methods and pathology* **88**: 284-292.

Lee S, Huen S, Nishio H, Nishio S, Lee HK, Choi BS, Ruhrberg C, Cantley LG. 2011. Distinct macrophage phenotypes contribute to kidney injury and repair. *Journal of the American Society of Nephrology : JASN* **22**: 317-326.

Lin SL, Castano AP, Nowlin BT, Lupher ML, Jr., Duffield JS. 2009. Bone marrow Ly6Chigh monocytes are selectively recruited to injured kidney and differentiate into functionally distinct populations. *J Immunol* **183**: 6733-6743.

Mishra J, Ma Q, Prada A, Mitsnefes M, Zahedi K, Yang J, Barasch J, Devarajan P. 2003. Identification of neutrophil gelatinase-associated lipocalin as a novel early urinary biomarker for ischemic renal injury. *Journal of the American Society of Nephrology : JASN* **14**: 2534-2543.

Mochizuki T, Lemmink HH, Mariyama M, Antignac C, Gubler MC, Pirson Y, Verellen-Dumoulin C, Chan B, Schroder CH, Smeets HJ et al. 1994. Identification of mutations in the alpha 3(IV) and alpha 4(IV) collagen genes in autosomal recessive Alport syndrome. *Nature genetics* **8**: 77-81.

Nabity MB, Lees GE, Cianciolo R, Boggess MM, Steiner JM, Suchodolski JS. 2012. Urinary biomarkers of renal disease in dogs with X-linked hereditary

nephropathy. *Journal of veterinary internal medicine / American College of Veterinary Internal Medicine* **26**: 282-293.

Ninichuk V, Gross O, Reichel C, Khandoga A, Pawar RD, Ciubar R, Segerer S, Belemezova E, Radomska E, Luckow B et al. 2005. Delayed chemokine receptor 1 blockade prolongs survival in collagen 4A3-deficient mice with Alport disease. *Journal of the American Society of Nephrology : JASN* **16**: 977-985.

Rodgers KD, Rao V, Meehan DT, Fager N, Gotwals P, Ryan ST, Koteliansky V, Nemori R, Cosgrove D. 2003. Monocytes may promote myofibroblast accumulation and apoptosis in Alport renal fibrosis. *Kidney international* **63**: 1338-1355.

Sampson NS, Ryan ST, Enke DA, Cosgrove D, Koteliansky V, Gotwals P. 2001. Global gene expression analysis reveals a role for the alpha 1 integrin in renal pathogenesis. *The Journal of biological chemistry* **276**: 34182-34188.

Temme J, Peters F, Lange K, Pirson Y, Heidet L, Torra R, Grunfeld JP, Weber M, Licht C, Muller GA et al. 2012. Incidence of renal failure and nephroprotection by RAAS inhibition in heterozygous carriers of X-chromosomal and autosomal recessive Alport mutations. *Kidney international* **81**: 779-783.

Van Rooijen N, Sanders A. 1994. Liposome mediated depletion of macrophages: mechanism of action, preparation of liposomes and applications. *Journal of immunological methods* **174**: 83-93.

van Rooijen N, Sanders A, van den Berg TK. 1996. Apoptosis of macrophages induced by liposome-mediated intracellular delivery of clodronate and propamidine. *Journal of immunological methods* **193**: 93-99.

Wang Y, Harris DC. 2011. Macrophages in renal disease. *Journal of the American Society of Nephrology : JASN* **22**: 21-27.

Whalen RE, Huang S, Peschel E, Mc IH. 1961. Hereditary nephropathy, deafness and renal foam cells. *The American journal of medicine* **31**: 171-186.

Wu X, Schulte BC, Zhou Y, Haribhai D, Mackinnon AC, Plaza JA, Williams CB, Hwang ST. 2014. Depletion of M2-like tumor-associated macrophages delays cutaneous T-cell lymphoma development in vivo. *The Journal of investigative dermatology* **134**: 2814-2822.

2

Characterization of DPP9 protease dead mutant mice

2.1 Introduction

Dipeptidyl peptidase 9 (DPP9) is an intracellular serine protease of largely unknown *in vivo* functions. DPP9 was identified *in silico* by Abbott et al. (Abbott et al. 2000) with the genomic structure cloned and characterized by Olsen and Wagtmann in 2002 (Olsen and Wagtmann 2002). As a member of DPP4 and S9b gene family, DPP9 and the related DPP4, DPP8, and Fibroblast Activation Protein (FAP) have a rare ability to cleave N-terminus of peptide substrates at post-proline bond in the penultimate position. A conserved catalytic triad of serine, aspartate, and histidine in an active site is essential for their activity and the unique substrate specificity (Abbott et al. 2000; Olsen and Wagtmann 2002; Ajami et al. 2004). Human DPP9 shares 93% and 94% amino acid similarity with mouse and rat DPP9, respectively. DPP8 is the closest relative of DPP9 with 79 % similarity and 61% identity in amino acid level (Ajami et al. 2004). DPP8 and DPP9 are localized to human chromosomes 15q22 and 19p13.3, respectively (Olsen and Wagtmann 2002). A high degree of homology together with the conservation of clusters of paralogous genes between human chromosomes 15q24→26 and 19p13.3→p12 (Carim-Todd et al. 2000) suggests that DPP8 and DPP9 arise in an ancestral duplication of a chromosomal segment. Biochemical properties of DPP8 and DPP9 are very similar including substrate specificity and catalytic efficiency against synthetic peptides (Bjelke et al. 2006; Geiss-Friedlander et al. 2009; Tang et al. 2009). Moreover, both can process DPP4 substrates glucagon-like peptide-1 (GLP-1), GLP-2, neuropeptide Y (NPY) and peptide YY in cell extract (Bjelke et al. 2006) and NPY in intact cells (Lu et al. 2011). Recently, adenylate kinase 2 and calreticulin were identified as natural substrate candidates for DPP8 and DPP9 using a cytosol-wide proteomic screen (Wilson et al. 2013). The remarkable substrate overlap together with no unique cleavage sites identified so far for DPP8 or DPP9, led to the speculation that

there may be functional redundancy between the two enzymes (Tang et al. 2009; Wilson et al. 2013).

A functional role of DPP9 in regulation of cell survival, migration and apoptosis emerges from *in vitro* studies, however, no supportive *in vivo* evidence has been provided so far. Impaired cell adhesion, migration and wound healing with increased spontaneous apoptosis independent of DPP9 enzyme activity is reported in DPP9 overexpressing HEK293T cells (Yu et al. 2006). siRNA mediated DPP9 knockdown and pharmacological inhibition of DPP9 enzyme in Huh7 cells leads to similar functional outcome with impaired cell adhesion and migration associated with decreased expression of adhesion signaling pathway in the absence of cell death (Zhang et al. 2015). Overexpression of enzyme active DPP9 in HepG2 and Huh7 cells attenuates epidermal growth factor (EGF)-mediated PI3K/Akt signaling resulting in augmented apoptosis and suppressed cell proliferation in HepG2 cells (Yao et al. 2011). On the contrary, DPP9 down-regulation enhanced NPY-induced cell death in Ewing sarcoma family of tumor (Lu et al. 2011) and DPP8/9 inhibition induced spontaneous apoptosis of primary macrophages in NPY independent manner (Matheeussen et al. 2013). Different and sometimes contradictory responses of DPP9 imply that the role of DPP9 varies depending on the cell type and the disease. DPP8 and DPP9 are ubiquitously expressed (Abbott et al. 2000; Olsen and Wagtmann 2002; Yu et al. 2009) including leukocytes (Ajami et al. 2004; Maes et al. 2007; Yu et al. 2009; Chowdhury et al. 2013) and upregulated in activated human and rodent lymphocytes (Bank et al. 2011; Chowdhury et al. 2013). Anti-proliferative effects of DPP8/9 inhibition are observed after activation of human and rodent T-cells *in vitro* (Lankas et al. 2005; Reinhold et al. 2009). Although, both DPP8 and DPP9 are expressed in macrophage-rich regions of human altherosclerotic plaques, only DPP9 is upregulated in monocytes differentiated macrophages and loss of DPP9 activity decreases proinflammatory cytokines secretion in activated macrophages *in vitro* (Matheeussen et al. 2013). Furthermore, the cytoplasmic $RU1_{34\text{-}42}$ antigenic peptide was recently identified as *in vivo* substrate for DPP9 but not DPP8 implying a role of DPP9 in antigen presentation (Geiss-Friedlander et al. 2009). *In vivo* study revealed immune toxicity attributed to DPP8/9 inhibition and associated with thrombocytopenia, reticulocytopenia and splenomegaly (Lankas et al. 2005). Contrary

to this, a different chemical class of cell permeable DPP8/9 inhibitors is reported to have a good safety profile in rodents (Wu et al. 2009). This further emphasizes the importance of selective targeting of DPP8 or DPP9 enzymes in shedding light on their biology. Recently published catalytically inactive DPP9 knock-in mice are neonatally lethal, the cause of which is unknown (Gall et al. 2013). This study was conducted to investigate the cause of neonatal death of DPP9 knock-in mice and the role of DPP9 enzyme in mouse immune system.

2.2 Results

Serine to alanine point mutation (S729A) in the catalytic domain of DPP9 gene results in loss of DPP9 enzymatic activity in mice

To assess the biological relevance of the DPP9 protease activity, we generated genetically modified mice by homologous recombination with a targeting vector carrying a TCC to GCC mutation encoding a catalytically inactive S729A mutant of the DPP9 protein (Figure 2.1A). Successfully targeted ES cells were identified by Southern blot (Figure 2.1B). Mice heterozygous for the mutation ($DPP9^{+/ki}$) were healthy and fertile, and crossed to obtain homozygous mice ($DPP9^{ki/ki}$). The mutant DPP9 gene was distinguished from the wild type DPP9 gene by genomic PCR genotyping (Figure 2.1C). To confirm that catalytically active DPP9 protein is indeed absent in $DPP9^{ki/ki}$ mice, DPP9 enzyme activity was measured in brain tissue homogenates from newborn mice (P1) because of the high DPP9 protein and mRNA expression in nervous system during mouse neonatal development as shown by others (Yu et al. 2009) and confirmed by our study (Figure 2.2). We utilized activity based proteomics with biotinylated fluorophosphonate referred to as FP-biotin used as an activity based probe (ABP). FP-biotin covalently binds to catalytic serine of active serine hydrolases in an activity-dependent manner and does not bind to proteolytically inactive enzymes (Liu et al. 1999). FP-biotin reactive proteins from mouse brain were selectively enriched using streptavidin beads and detected by SDS-PAGE/western blot using specific antibodies. As shown in Figure 2.1D, anti-DPP9, DPP8 and PEP antibodies recognized the respective human recombinant proteins (lane 1-3). ABP pull down of human DPP9 (lane 4) and DPP8 (lane 5) recombinant proteins, used to validate the assay, confirmed the detection of active serine proteases. In ABP pull

down of DPP9$^{+/+}$ mouse brain lysate, two proteins at 98kDa and 100kDa are identified with anti-DPP9 antibody (lane 6). 98kDa protein was absent while 100kDa protein remained in ABP pulled down of DPP9$^{ki/ki}$ mouse brain lysate (lane 7).

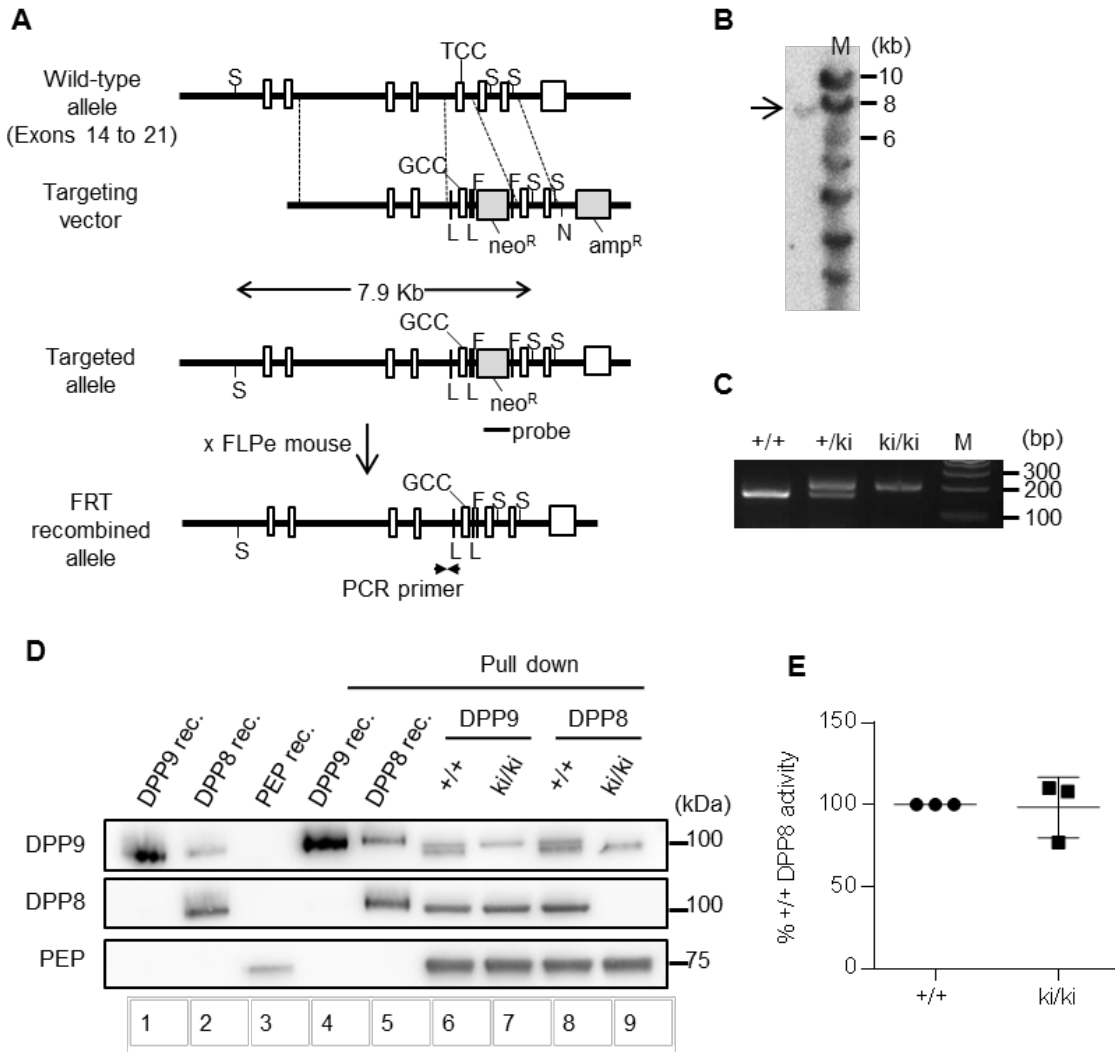

Figure 2.1. Loss of DPP9 enzymatic activity in mice by serine to alanine point mutation (S729A) in the catalytic domain of DPP9 gene. (**A**) Generation of DPP9$^{ki/ki}$ mice. The targeting vector carries a TCC→ GCC mutation (nucleotide 97 – 99 of exon 18 of the DPP9 gene) leading to a S729A mutation in the DPP9 protein. A neomycin resistance gene (neo^{R}), flanked by flippase recombinase target (F) sites, is removed by crossing with flippase recombinase expressing mice. Southern probe, PCR primers used for screening recombinant ES cells and genotyping are indicated. Restriction enzyme cleavage sites: S, SacI; N, NotI. Recombinase specific sites: L, LoxP; F, FRT. (**B**) Southern blot of Sac I-digested genomic DNA from the targeted ES cells. Predicted size of the DNA fragment is 7890 bp. M: marker. (**C**) PCR genotyping with set of primers that flank the loxP sites of targeted allele give a product of 180bp in DPP9$^{+/+}$, 200bp in DPP9$^{ki/ki}$, and 180bp and 200bp in DPP9$^{+/ki}$ mice.

Since DPP9 and DPP8 are highly homologous proteins and anti-DPP9 antibody cross react with human DPP8 recombinant proteins (lane 2), we speculated that the remaining 100kDa band represents active DPP8 protein. To test this hypothesis, we utilized DPP8 S749A knock-in mice ($DPP8^{ki/ki}$) which were generated using the similar strategy as $DPP9^{ki/ki}$ mice. Indeed, in ABP pull down of $DPP8^{ki/ki}$ mouse brain lysate, 100kDa band (lane 9) was absent when detected with anti-DPP8 antibody while 98kDa protein remained and was detected with anti-DPP9 antibody (line 9). These results demonstrate that 98kDa and 100kDa bands represent active DPP9 and DPP8 protein, respectively. Furthermore, no compensatory upregulation by DPP8 active enzyme was detected in $DPP9^{ki/ki}$ brains as demonstrated by similar levels of DPP8 enzyme activity in $DPP9^{+/+}$ and $DPP9^{ki/ki}$ brain lysates (Figure 2.1E). Taken together, these data demonstrate loss of DPP9 enzymatic activity and the lack of compensatory regulation by DPP8 enzymatic activity in newborn $DPP9^{ki/ki}$ mice.

Neonatal lethality due to suckling defect in $DPP9^{ki/ki}$ mice

$DPP9^{ki/ki}$ mice were born at the expected Mendelian ratio, but died during the first postnatal day (P1) (Figure 2.3A). The overt appearance of newborn $DPP9^{ki/ki}$ mice was normal. They were able to breathe and move, suggesting no overt respiratory and sensory motor defects. However, body weight of $DPP9^{ki/ki}$ mice measured at ~12 h after birth was lower (~7.5%) compared to $DPP9^{+/+}$ littermates (Figure 2.3B).

(**D**) Loss of DPP9 enzymatic activity in $DPP9^{ki/ki}$ mouse brain lysate detected with activity-based probe (ABP). Anti-DPP9, DPP8 or PEP antibodies recognize human recombinant proteins at ~ 98, 100, and 75 kDa, respectively (lane 1-3). PEP is used as a loading control. ABP pull down using human DPP9 and DPP8 recombinant proteins as positive controls detects enzymatically active recombinant proteins (lane 4, 5). Anti-DPP8 antibody detects DPP8 recombinant protein only (lane 2, 5) in contrast to anti-DPP9 antibody which recognizes both DPP8 and DPP9 recombinant proteins (lane 2, 4, 5). In ABP pull down of wild-type brain lysate two bands (~ 98kDa and 100kDa) are detected with anti-DPP9 antibody and one band (~ 100kDa) with anti-DPP8 antibody (lane 6, 8). 98kDa band is absent in ABP pull down of $DPP9^{ki/ki}$ brain lysates (lane 7) and 100kDa band is absent in ABP pull down of $DPP8^{ki/ki}$ brain lysates (lane 9) demonstrating that 98kD and 100kDa band represent enzymatically active DPP9 and DPP8, respectively and that enzymatically active DPP9 is absent in $DPP9^{ki/ki}$ mice. (**E**) Comparable DPP8 enzymatic activity in $DPP9^{ki/ki}$ and $DPP9^{+/+}$ brain at P1 analyzed by quantitative assessment of ABP assay.

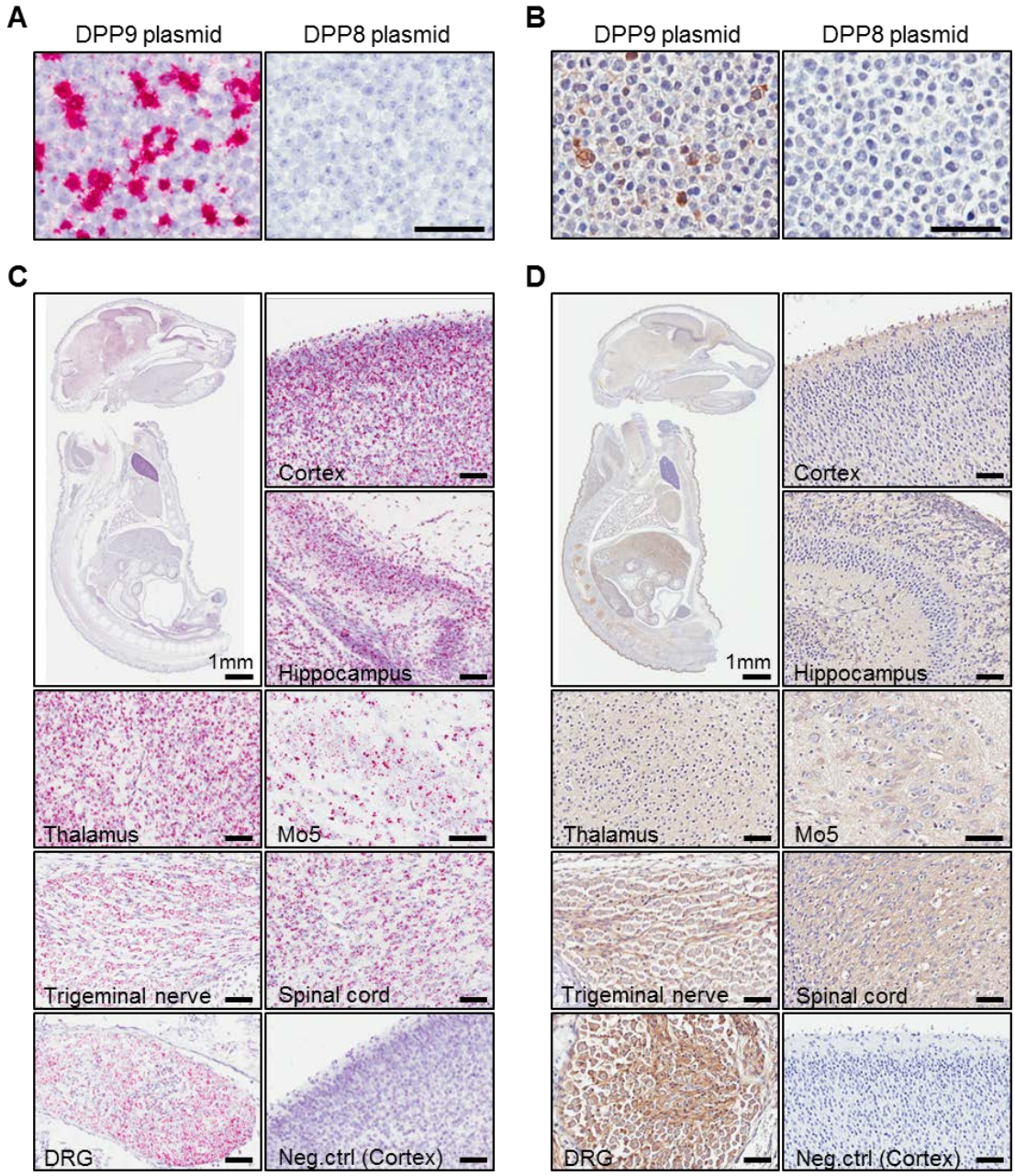

Figure 2.2. High DPP9 mRNA and protein expression in mouse nervous system at P1. (**A, B**) Specificity of DPP9 antisense probe (**A**) anti-DPP9 antibody (**B**) is validated by *in situ* hybridization and immunohistochemistry in HEK293 cells transfected with mouse DPP8 or DPP9. (**C**) *In situ* hybridization analysis of DPP9 mRNA expression in P1 wild-type mouse reveals high DPP9 expression in nervous system structures including brain (as shown for cortex, hippocampus, thalamus, and Mo5), trigeminal nerve, spinal cord, and DRG. (**D**) High DPP9 protein signal in P1 wild-type mouse nervous system structures including brain (as shown for cortex, hippocampus, thalamus, and Mo5), trigeminal nerve, spinal cord, and DRG by immunohistochemistry. Mo5, trigeminal motor nucleus; DRG, dorsal root ganglion. Scale bars: 50 µm (unless stated otherwise).

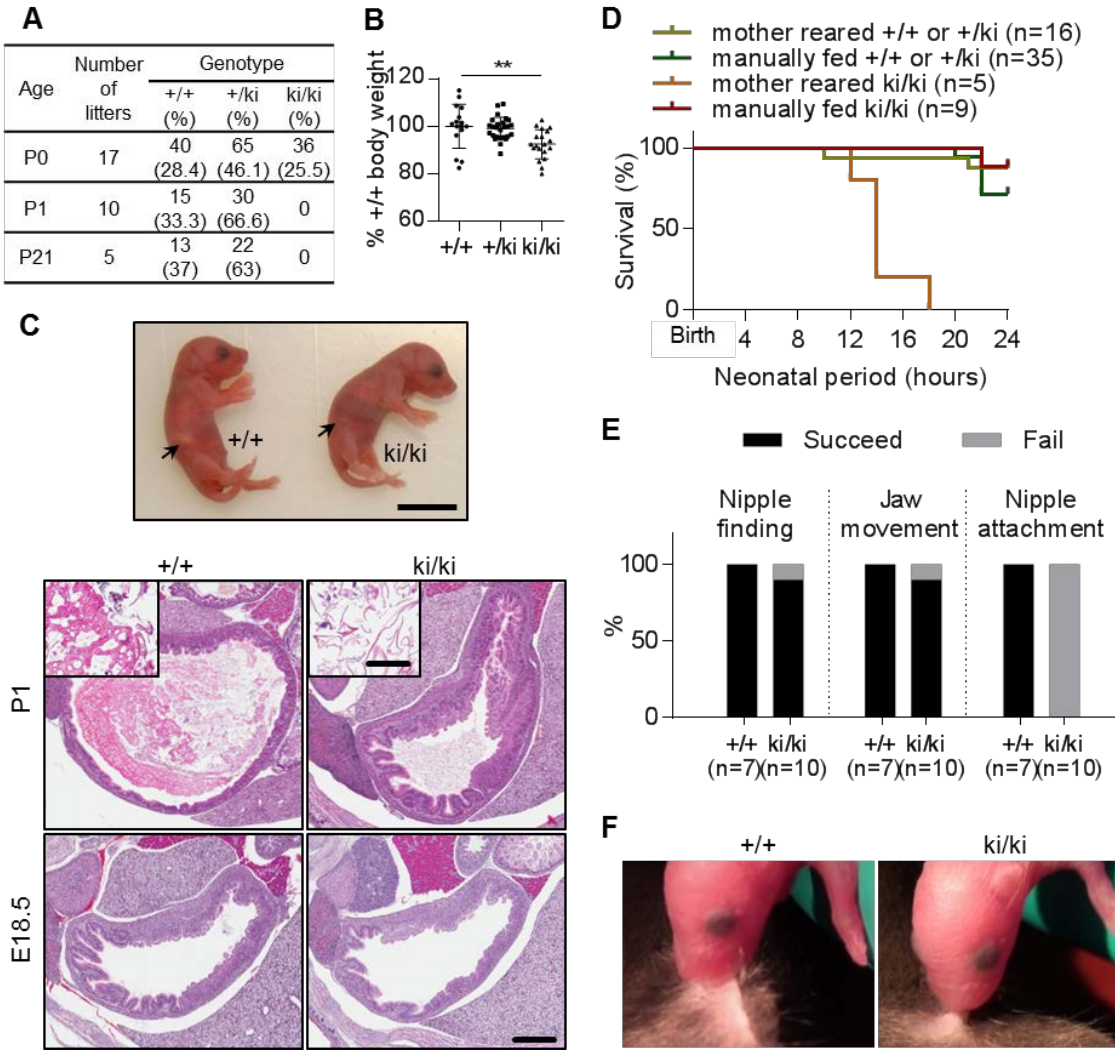

Figure 2.3. DPP9$^{ki/ki}$ mice die shortly after birth due to impaired suckling response. (**A**) DPP9$^{ki/ki}$ mice are born at the expected Mendelian ratio but do not survive the first postnatal day (P1). P0, time of birth. (**B**) Body weight of DPP9$^{ki/ki}$ mice measured at ~12 h after birth is slightly lower than that of DPP9$^{+/+}$ littermates. (**C**) DPP9$^{ki/ki}$ newborn mice, unlike DPP9$^{+/+}$ littermates, lack milk in the stomach (arrow) as visualized macroscopically and on H&E-stained sections. Inset shows presence of milk in DPP9$^{+/+}$ and its absence in DPP9$^{ki/ki}$ mice which contain in stomach only exfoliating epithelial cells. Stomach develops normally in DPP9$^{ki/ki}$ mice as analyzed on E18.5 and P1. Scale bar upper panel: 1 cm, lower panel: 500 µm, inset: 50 µm. (**D**) Rescue of DPP9$^{ki/ki}$ mice by hand feeding. DPP9$^{ki/ki}$ mice manually fed every 2 h for 24 h survive during the entire duration of the study in contrast to mother reared DPP9$^{ki/ki}$ mice which die within 12-18 h after birth. (**E**) Analysis of suckling behavior reveals defects in nipple attachment but normal nipple finding and jaw movement responses in newborn DPP9$^{ki/ki}$ mice. (**F**) Snapshots of video recording demonstrate weak attachment of newborn DPP9$^{ki/ki}$ mice to mother's nipple while being pulled away from mother.

Furthermore, all DPP9$^{ki/ki}$ mice lacked milk in their stomachs even within 18 h after birth as demonstrated visually by the absence of the milk spot and on H&E-stained stomach sections (Figure 2.3C). Only exfoliated epithelial cells and mucus were observed in stomach of newborn DPP9$^{ki/ki}$ mice, their stomach, however, developed normally as shown by the analysis of E18.5 embryos (Figure 2.3C). To examine whether the neonatal lethality of DPP9$^{ki/ki}$ mice is caused by defects in suckling response, newborn mice were separated from the mother and manually fed with artificial cat milk every 2 h for 24 h. Manually-fed DPP9$^{ki/ki}$ mice survived during the entire experimental period whereas mother-reared DPP9$^{ki/ki}$ mice died within 12-18 h after birth, demonstrating that suckling defect is the primary cause of neonatal lethality of DPP9$^{ki/ki}$ mice (Figure 2.3D). Abnormal suckling response can be a consequence of defects in energy homeostasis (Turgeon and Meloche 2009). Comparable fasted blood glucose levels measured at 3 h after birth with 54 ± 15 mg/dL vs 61 ± 14 mg/dL in DPP9$^{+/+}$ and DPP9$^{ki/ki}$ mice, respectively indicated, however, normal energy level in DPP9$^{ki/ki}$ mice. The suckling response is a complex behavior that includes finding mother's nipple, nipple attachment, suckling with rhythmic movements of the jaw and tongue, and milk withdrawal (Blass and Teicher 1980). To examine the feeding behavior, DPP9$^{ki/ki}$ and littermates pups were placed alone with anesthetized mother to feed and video recorded. DPP9$^{ki/ki}$ pups were able to locate nipple and showed rhythmic jaw movements indicating normal development of olfactory and sensory-motor system involved in suckling response (Figure 2.3E). In accordance with this, E10.5 DPP9$^{ki/ki}$ embryos showed well preserved gross morphology of trigeminal sensory nerve (V) and glossopharyngeal sensory nerve (IX) which relay sensation from the face and the tongue (Figure 2.4A). Furthermore, discrete neuronal patterns (barrelettes) were formed in spinal trigeminal nucleus from newborn DPP9$^{ki/ki}$ mice indicating normal interaction between the primary vibrissal afferents and second-order neurons innervating tactile sensation of face (Figure 2.4B). Comparable populations of motor neurons in brainstem nuclei innervating jaw (trigeminal motor nucleus; Mo5), face (facial motor nucleus; 7N), and tongue (hypoglossal nucleus; 12N) muscles (Figure 2.4C) together with normal development of neuromuscular junctions in masseter and tongue muscles of DPP9$^{ki/ki}$ newborn mice (Figure 2.4D and E) provide evidence that motor system is intact in DPP9$^{ki/ki}$ mice.

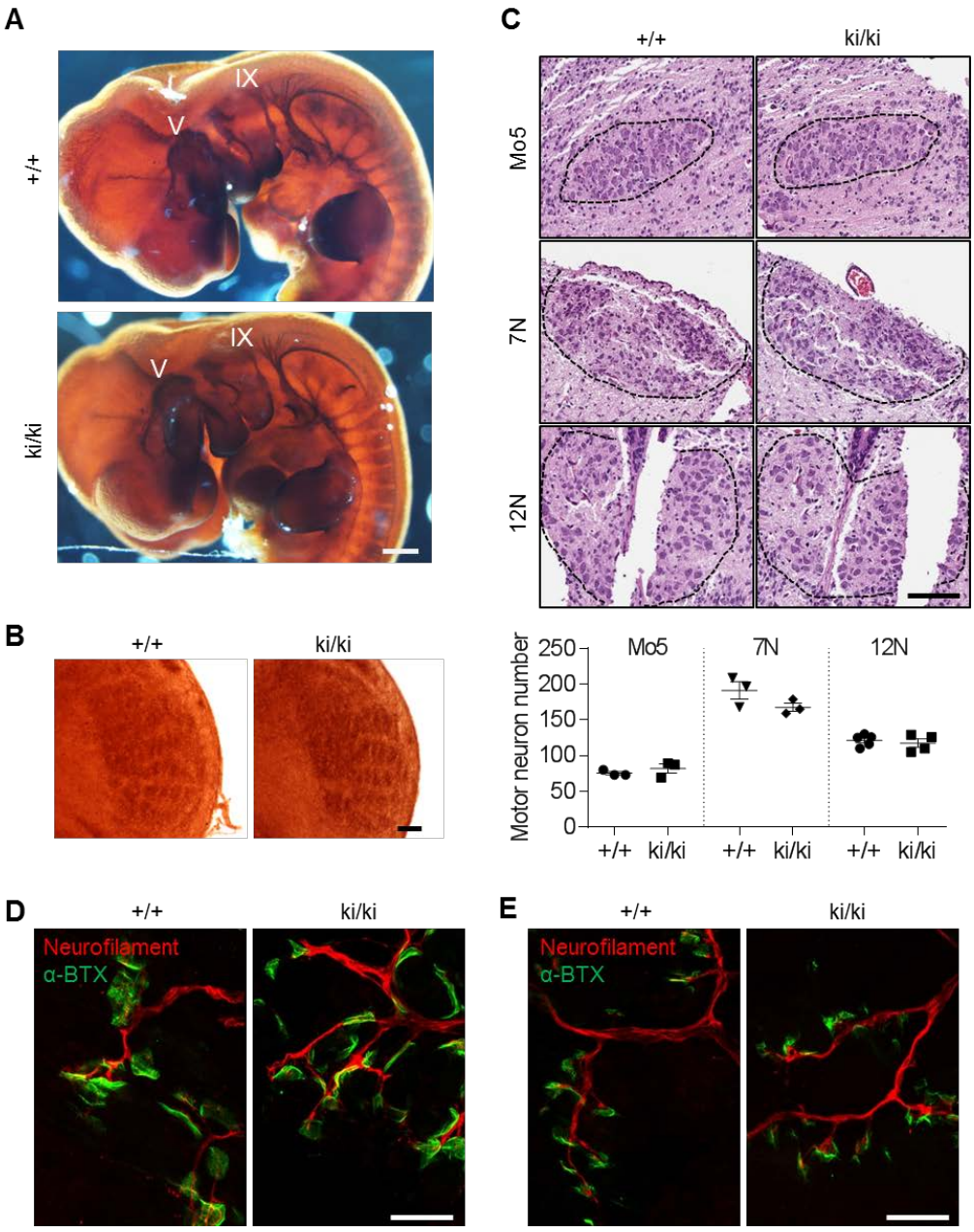

Figure 2.4. Normal development of sensory and motor neuronal pathways in DPP9$^{ki/ki}$ mice. (**A**) Normal cranial nerve development in DPP9$^{ki/ki}$ at E10.5. Whole-mount neurofilament staining demonstrates the location and normal morphology of cranial nerves (V, trigeminal; IX, glossopharyngeal). Scale bar: 500 µm. (**B**) Cytochrome oxidase staining in spinal trigeminal nucleus reveals normal formation of whisker-related barrelettes in newborn DPP9$^{ki/ki}$ mice. Scale bar: 100 µm (**C**) Brainstem motor neurons develop normally in DPP9$^{ki/ki}$ newborn mice as shown on representative images and quantitative analysis of motor neuron populations (Mo5, trigeminal motor nucleus; 7N, facial motor nucleus, 12N, hypoglossal motor nucleus). Scale bar: 100 µm (**D, E**) The morphology of neuromuscular junctions is grossly normal in DPP9$^{ki/ki}$ newborn mice as shown by immunofluorescence staining of axonal neurofilaments and α-BTX staining of postsynaptic nAChRs in masseter (**D**) and tongue (**E**) muscles. Scale bars: 50 µm

In contrast to the normal nipple finding and normal jaw movement, DPP9$^{ki/ki}$ mice displayed defects in nipple attachment (Figure 2.3E). DPP9$^{ki/ki}$ mice were unable to attach well to mother's nipple and did not stretch the nipple when they were pulled away from the mother (Figure 2.3E and F) implicating potential craniofacial abnormalities as a cause of suckling defects.

Microglossia with intrinsic distal tongue muscle defects in DPP9$^{ki/ki}$ mice

The examination of craniofacial structures revealed reduced tongue size in newborn DPP9$^{ki/ki}$ mice as visualized macroscopically and quantified by surface area measurement (Figure 2.5A). H&E-stained frontal sections of P1 heads confirmed shorter (Figure 2.5B, level a) and smaller (Figure 2.5B, lever b) tongue in DPP9$^{ki/ki}$ mice as compared to DPP9$^{+/+}$ littermates, whereas the size of other structures including nasal cavity was comparable between the groups (Figure 2.5B). Histological evaluation of the tongue revealed that longitudinal muscle fibers in distal intrinsic tongue muscle failed to develop in newborn DPP9$^{ki/ki}$ mice (Figure 2.5C). Defects were restricted to distal intrinsic tongue muscle since the two other types of tongue muscles including extrinsic and proximal intrinsic muscles formed normally in DPP9$^{ki/ki}$ mice (Figure 2.5C). Similarly, normal masseter muscle was found in newborn DPP9$^{ki/ki}$ mice (Figure 2.5B, arrow). The reduced tongue size in DPP9$^{ki/ki}$ mice was already evident at E12.5, demonstrating that DPP9 enzymatic activity is required for normal tongue development (Figure 2.5D). Cleft palate, the frequently observed craniofacial defect linked to suckling related neonatal lethality, was not present in DPP9$^{ki/ki}$ mice which displayed normal fusion of palatal shelves (Figure 2.5B, asterisk).

We also investigated whether DPP9$^{+/ki}$ mice display any craniofacial abnormalities knowing that in heterozygous mice 80% of DPP9 enzymatic activity is inhibited as demonstrated by ABP pull down of brain tissue at P1 (Figure 2.6A). The tongue size analysis performed in newborn and 25 weeks old DPP9$^{+/ki}$ mice did not reveal any tongue defects (Figure 2.5A and 2.6B), thus indicating that the remaining 20% of DPP9 enzymatic activity is sufficient for normal tongue development. To further exclude any potential impairments in tongue function, body weight and food intake were measured weekly from the age of 5 weeks until the age of 25 weeks in DPP9$^{ki/+}$

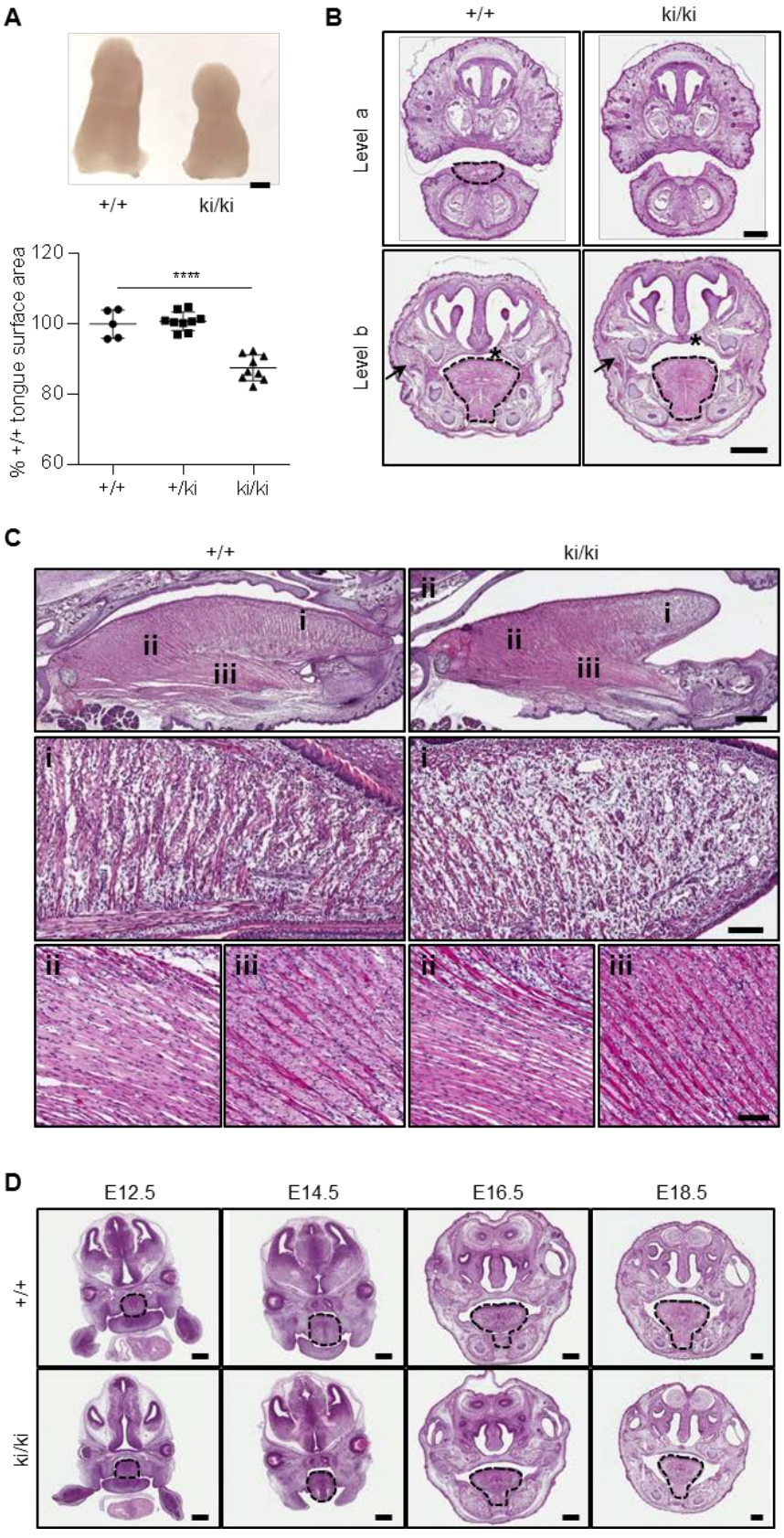

Figure 2.5. DPP9$^{ki/ki}$ mice exhibit microglossia with impaired intrinsic distal tongue muscle formation.

and DPP9$^{+/+}$ mice. As shown in figure 2.6C and D, DPP9$^{ki/+}$ mice were indistinguishable from control mice in all assessed parameters.

Reduced number and impaired survival of migratory tongue muscle progenitors in DPP9$^{ki/ki}$ mice

During the tongue development, extrinsic tongue muscles and proximal intrinsic tongue muscles derive from the head mesenchyme, whereas the distal intrinsic tongue muscles are formed mainly by migratory muscle progenitors that derive from the somites at occipital level (Huang et al. 1999; Vasyutina et al. 2005). Since DPP9$^{ki/ki}$ mice showed impaired formation of distal intrinsic tongue muscles, we next examined the migratory tongue muscle progenitors. It is well documented that muscle precursors at occipital, cervical and limb levels delaminate from lateral dermomyotome, a derivative of the somite, and actively migrate to their target sites to generate tongue, diaphragm, and limb muscles, respectively (Chevallier et al. 1977; Christ et al. 1977; Christ and Ordahl 1995). The homeobox gene Lbx1 is exclusively expressed in dermomyotomes of occipital, cervical and limb levels where it specifically marks migratory muscle precursors (Dietrich et al. 1999). We reconstructed the migration stream of tongue muscle progenitors in DPP9$^{+/+}$ and DPP9$^{ki/ki}$ embryos by staining the consecutive E10.75 sections with Lbx1 antibody. In both, DPP9$^{+/+}$ and DPP9$^{ki/ki}$ embryos, a stream of Lbx1^{+} muscle progenitors was observed in the hypoglossal cord and in the first branchial arch, which is the route and the target area of the migratory cells, respectively (Figure 2.7A). Quantification of Lbx1^{+} area revealed significantly

(**A**) Reduced tongue size in DPP9$^{ki/ki}$ newborn mice visualized macroscopically and quantified by surface area measurement. Scale bar: 1 mm (**B**) H&E-stained frontal head sections show shorter (level a) and smaller (level b) tongue in DPP9$^{ki/ki}$ newborn mice compared to DPP9$^{+/+}$ littermates. Formation of masseter muscle (arrow) and palate (asterisk) are normal in DPP9$^{ki/ki}$ newborn mice. Dashed lines indicate outline of the tongue. Scale bar upper panel: 500 µm, lower panel: 1 mm. (**C**) DPP9$^{ki/ki}$ mice lack longitudinal muscle fibers in intrinsic distal tongue muscle (i) whereas intrinsic proximal (ii) and extrinsic (iii) tongue muscles develop normally. Middle and bottom panels show magnified view of respective muscles. Scale bar top panel: 500 µm, middle and bottom panels: 100 µm. (**D**) In DPP9$^{ki/ki}$ mice, reduced tongue size is evident as early as E12.5 and remains through the development as shown on H&E-stained frontal head sections. Scale bars: 500 µm.

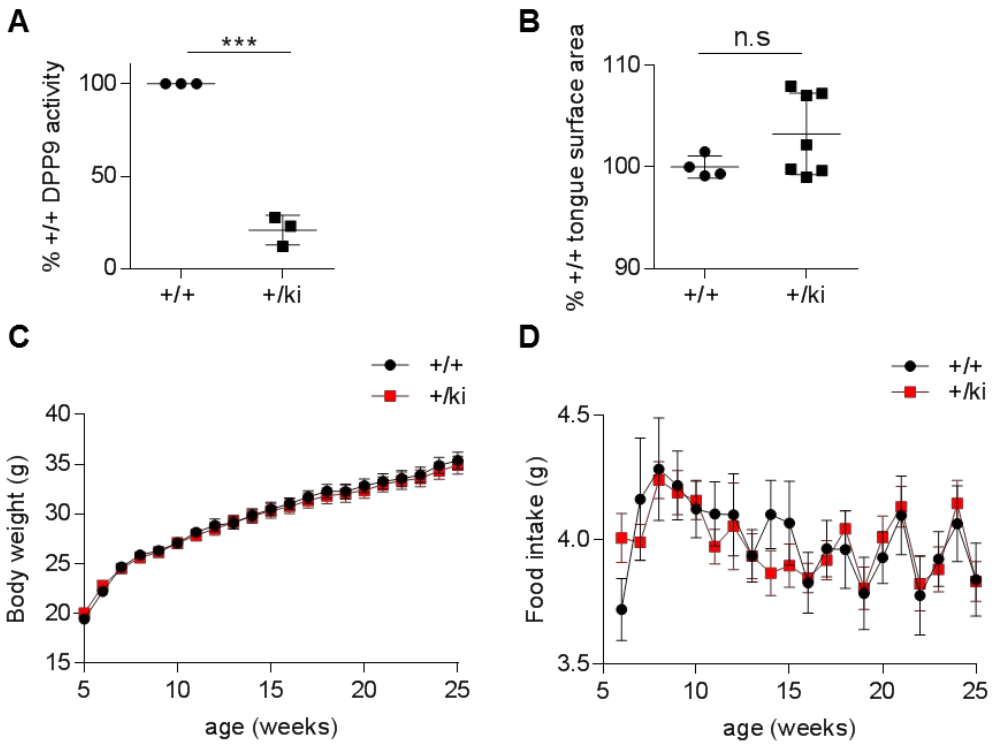

Figure 2.6. Normal tongue size, food intake and body weight in DPP9$^{+/ki}$ mice. (**A**) reduction of DPP9 enzymatic activity is reduced by ~80% in DPP9$^{+/ki}$ compared to DPP9$^{+/+}$ brains at P1 as shown by quantitative assessment of ABP assay. (**B**) Tongue surface area measurement shows similar tongue size in DPP9$^{+/+}$ and DPP9$^{+/ki}$ mice at the age of 25 weeks. (**C, D**) Body weight evolution (**C**) and food intake (**D**) are comparable between DPP9$^{+/+}$ and DPP9$^{+/ki}$ from 5 till 25 weeks of age.

decreased number of migratory tongue muscle progenitors in DPP9$^{ki/ki}$ embryos compared to DPP9$^{+/+}$ littermates (Figure 2.7A). The reduction in Lbx1^{+} muscle progenitors was accompanied by an increased spontaneous apoptosis in both the hypoglossal cord and the first branchial arch as shown by elevated cleaved caspase 3 signals (Figure 2.7B). The analysis of limb muscles, known also to derive from Lbx1^{+} migratory muscle progenitors, showed comparable number of Lbx1^{+} cells and no difference in the apoptosis between DPP9$^{ki/ki}$ and DPP9$^{+/+}$ littermates at E10.75 (Figure 2.7C). These results demonstrate that DPP9 enzymatic activity is crucial for the survival of tongue muscle progenitors but has no effect on other migratory muscle progenitors. Analysis of DPP9 protein expression in E10.75 wild type mice revealed ubiquitous expression including Lbx1^{+} migratory tongue muscle progenitors in the hypoglossal cord and the first branchial arch (Figure 2.7D). Furthermore, although DPP9 is highly expressed at neural tube at E10.75 (Figure 2.7E), no changes were

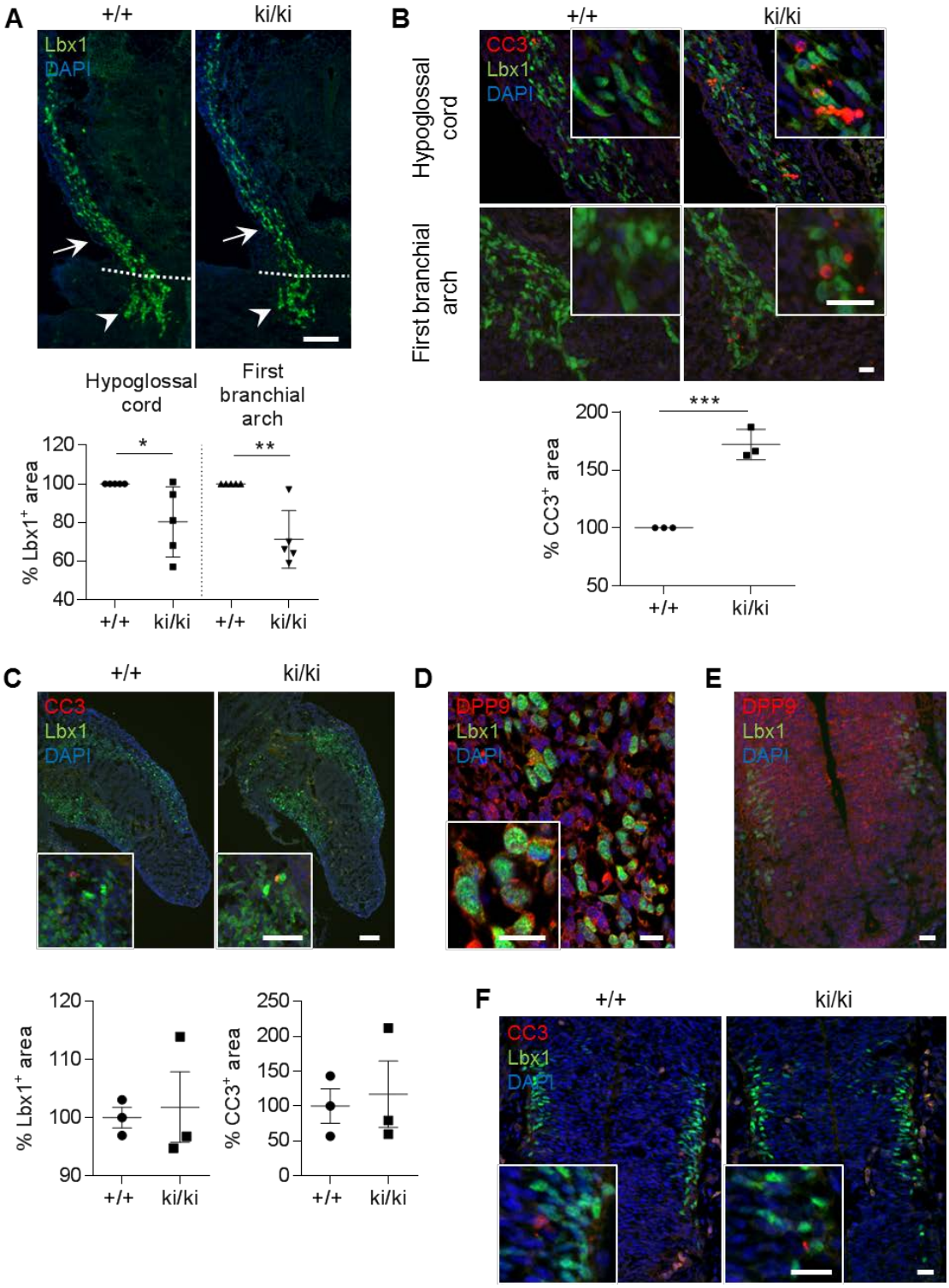

Figure 2.7. Migration of tongue muscle progenitors along the hypoglossal cord to first branchial arch is associated with reduced number of Lbx1^{+} progenitors and increased apoptosis in DPP9$^{ki/ki}$ embryos at E10.75.

observed in the number of $Lbx1^+$ cells and/or apoptosis in neural tube from $DPP9^{ki/ki}$ mice at E10.75 (Figure 2.7F).

CXCR4 and its ligand SDF-1, expressed in the hypoglossal cord and the first branchial arch, respectively, are required for migration and survival of migratory hypaxial muscle progenitors (Vasyutina et al. 2005). In CXCR4-deficient mice, reduced number of muscle progenitors at the first branchial arch and dorsal limb is observed, and it is accompanied by increased apoptosis (Vasyutina et al. 2005).Therefore, next we examined expression of CXCR4 protein in migratory muscle progenitors from $DPP9^{ki/ki}$ mice. No obvious differences were observed in CXCR4 staining in the hypoglossal cord and the first branchial arch in $DPP9^{ki/ki}$ and $DPP9^{+/+}$ mice at E10.75 (Figure 2.8A). In addition, since CXCR4 is Gi coupled receptor, we measured cAMP level upon SDF-1 treatment in HEK293 cells stably expressing CXCR4 transfected with wild type DPP9 plasmid (wtDPP9) or enzyme-inactive S729A mutant DPP9 plasmid (mutDPP9). Increased production of cAMP by forskolin was reduced upon SDF-1 treatment in CXCR4 stable cell line overexpressing wtDPP9 or mutDPP9 in a similar extent, demonstrating that absence of DPP9 enzyme does not impair CXCR4 signaling (Figure 2.8B). Compared to non-transfected cells, slight reduction in cAMP level was observed in cells overexpressing wtDPP9 plasmid upon forskolin treatment. This can be due to the transfection itself or an effect of DPP9 on cAMP formation which is independent of CXCR4 signaling. Furthermore, overexpression of enzyme inactive DPP9 in CXCR4 stable cell line show normal membrane localization of CXCR4 (Figure 2.8C). In conclusion, reduced survival of migratory tongue muscle

(**A**) Reduced number of $Lbx1^+$ muscle progenitors in the hypoglossal cord (arrow) and the first branchial arch (arrowhead) in $DPP9^{ki/ki}$ mice compared to $DPP9^{+/+}$ littermates is shown on representative images and by quantitative assessment of $Lbx1^+$ area in the reconstructed regions of interest. Scale bar: 100 µm. (**B**) Increased apoptosis analyzed by cleaved caspase-3 (CC3) in hypoglossal cord and the first branchial arch along the $Lbx1^+$ area in $DPP9^{ki/ki}$ mice compared to $DPP9^{+/+}$ littermates. Representative images and quantitative assessment of cleaved caspase 3^+ area in both hypoglossal cord and first branchial arch are shown. Scale bars: 20 µm. (**C**) In forelimbs, comparable levels of $Lbx1^+$ and cleaved caspase-3^+ cells are observed in $DPP9^{ki/ki}$ and $DPP9^{+/+}$ littermates. Scale bars: 100 µm. (**D**-**E**) Ubiquitous expression of DPP9 protein including $Lbx1^+$ cells along the hypoglossal cord (**D**) and the neural tube (**E**) in wild-type embryos at E10.75. Scale bars D: 10 µm, E: 20 µm. (**F**) In the neural tube, comparable levels of $Lbx1^+$ and cleaved caspase-3^+ cells are observed in $DPP9^{ki/ki}$ and $DPP9^{+/+}$ littermates. Scale bars: 20 µm.

progenitors is observed in DPP9$^{ki/ki}$ mice while loss of DPP9 enzymatic activity had no effect on other types of migratory hypaxial muscle progenitors. Furthermore, effects of DPP9 did not involve the modulation of CXCR4 signaling pathway.

Impaired fetal hematopoiesis but functional hematopoietic cells in DPP9$^{ki/ki}$ mice

Human and rodent leukocytes and immune organs express DPP9 and have DPP8/9 activity as published (Ajami et al. 2004; Maes et al. 2007; Yu et al. 2009; Chowdhury et al. 2013) and shown by our study (Figure 2.9A and B). Furthermore, DPP9 is shown to regulate immune function *in vitro* and *in vivo* (Lankas et al. 2005; Reinhold et al. 2009). In order to investigate the role of DPP9 in the immune system, we characterized the immune-related phenotype of DPP9$^{ki/ki}$ mice. Peripheral blood analysis of newborn

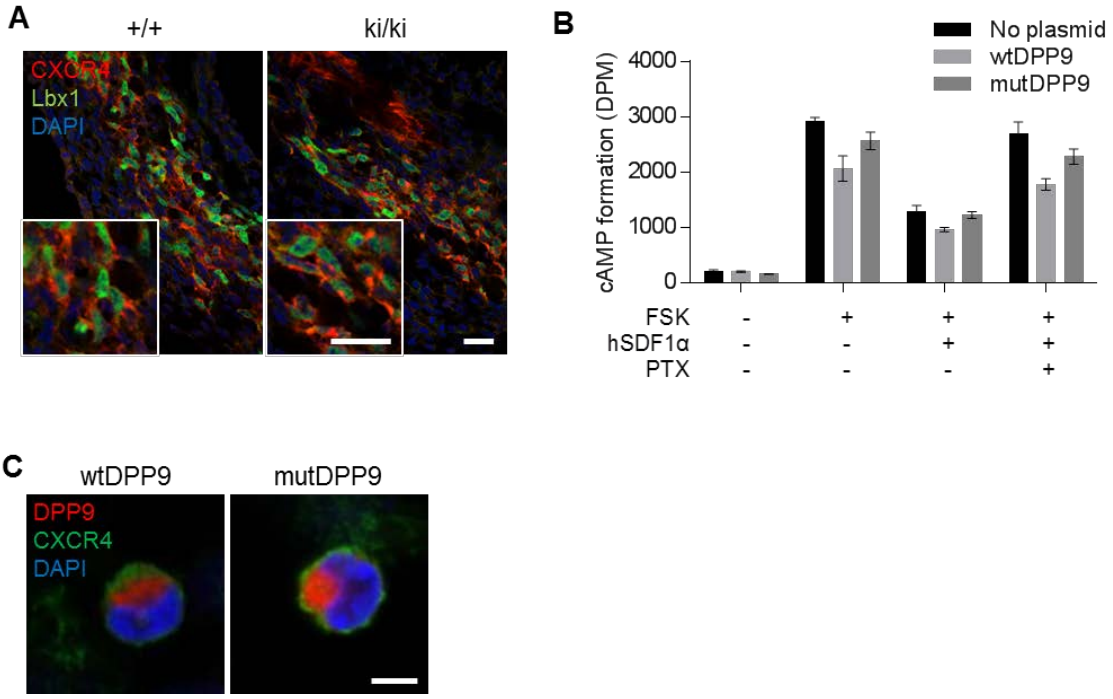

Figure 2.8. Normal CXCR4 signaling in the absence of DPP9 enzymatic activity. (**A**) Comparable distribution of CXCR4 protein in Lbx1^{+} cells in hypoglossal cord from DPP9$^{ki/ki}$ and DPP9$^{+/+}$ littermates at E10.75. Scale bars: 20 µm. (**B**) Inactivation of DPP9 enzymatic activity does not alter CXCR4-mediated Gi signaling upon hSDF-1α treatment. Similar level of cAMP reduction upon SDF-1α treatment is observed in CXCR4 stable cell line transfected with wtDPP9 plasmid or mutDPP9 plasmid. Forskolin is applied to increase cAMP formation and pertussis toxin to reverse Gi-coupled signaling. DPM, disintegrations per minute. (**C**) Similar distribution of CXCR4 in CXCR4 stable cell line transfected with either wtDPP9 or mutDPP9 plasmid. Scale bar: 5 µm.

DPP9$^{ki/ki}$ mice showed reduced number of lymphocytes and monocytes compared to DPP9$^{+/+}$ littermates, whereas another cell types including erythrocytes or granulocytes were not changed (Figure 2.10A and data not shown). Next, since i) liver is the primary hematopoietic organ from E11 until the first postnatal week and ii) DPP9 mRNA is expressed in newborn mouse liver hematopoietic cells (Figure 2.9C), we analyzed livers of E17.5 embryos by flow cytometry. Number of B220^{+}CD43^{+} pro-B cells, CD18^{+}CD11b^{+} and Gr-1^{+}CD11b^{+} myeloid cells were reduced in DPP9$^{ki/ki}$ fetal livers compared to DPP9$^{+/+}$ fetal livers (Figure 2.10B). These data demonstrate hematopoiesis defects in DPP9$^{ki/ki}$ mice during the development.

Reconstitution of lethally irradiated mice with fetal liver cells is useful to study the hematopoiesis of neonatal lethal animals (Eckardt and McLaughlin 2008). To further investigate the role of DPP9 enzyme in hematopoiesis, we have reconstituted lethally irradiated wild-type mice with DPP9$^{+/+}$ or DPP9$^{ki/ki}$ fetal liver cells. DPP9$^{ki/ki}$ fetal liver cells successfully reconstituted immune system of recipients as DPP9$^{+/+}$ fetal liver cells (data not shown). To avoid potential compensation of DPP8 enzyme, highly homologous with DPP9 and expressed in immune cells (Figure 2.9A), we performed competitive reconstitution assay. Fetal liver cells from E17.5 DPP9$^{+/+}$ and DPP9$^{ki/ki}$ embryos (CD45.2) were injected into lethally irradiated wild-type recipient mice (CD45.1) together with an equal number of competitor fetal liver cells from wild-type E17.5 embryos (CD45.1) (Figure 2.10C). Cells from bone marrow, spleen and thymus of recipient mice were analyzed by flow cytometry 6 weeks after the reconstitution. As shown in figure 2.10D, DPP9$^{ki/ki}$ CD45.2^{+} cells were detected in bone marrow, spleen and thymus of recipients with similar frequency as DPP9$^{+/+}$ CD45.2^{+} cells. Further staining with surface markers revealed that contribution of DPP9$^{ki/ki}$ CD45.2^{+} fetal liver cells to reconstitution of subpopulation of immune cells in recipient mice is comparable to that of DPP9$^{+/+}$ CD45.2^{+} fetal liver cells, implying the full potential of DPP9$^{ki/ki}$ fetal liver cells to differentiate into lymphoid and myeloid lineages (Figure 2.10E). In summary, these data demonstrate impaired hematopoiesis in DPP9$^{ki/ki}$ mice but normal ability of DPP9$^{ki/ki}$ hematopoietic stem cells to reconstitute functional immune system. Thus providing the evidence that DPP9 enzymatic activity in hematopoietic stem cells is not essential for normal hematopoiesis in mice.

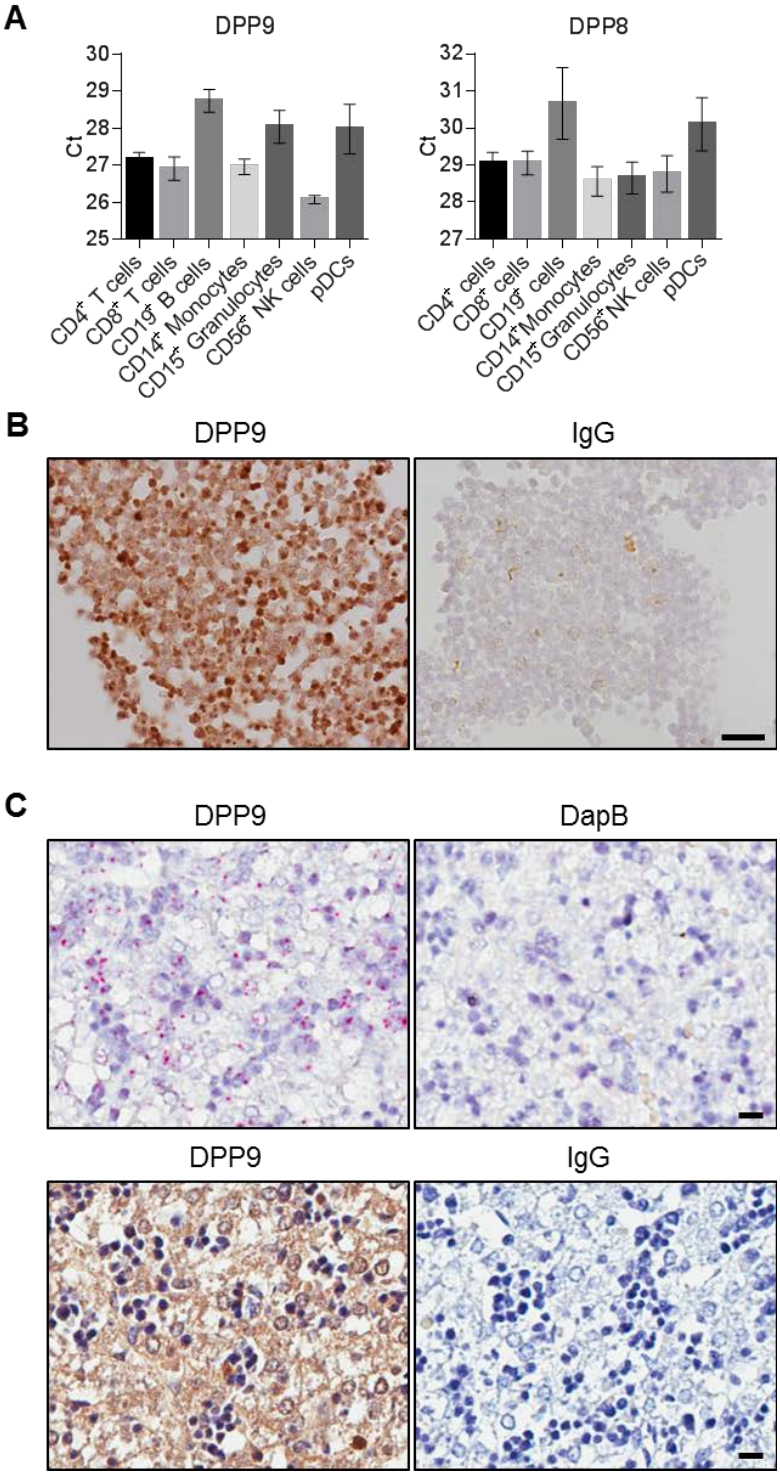

Figure 2.9. DPP9 is expressed in human blood immune cells and mouse liver hematopoietic cells. (**A**) Expression of DPP9 and DPP8 mRNA in subsets of purified human immune cells determined by Real-time PCR. (**B**) Immunohistochemical analysis of DPP9 expression in purified human $CD45^+$ leukocytes. Scale bar: 20 µm. (**C**) DPP9 is expressed in mouse liver hematopoietc cells at P1 as shown by *in situ* hybridization (upper panel) and immunohistochemistry (lower panel). Scale bars: 10 µm.

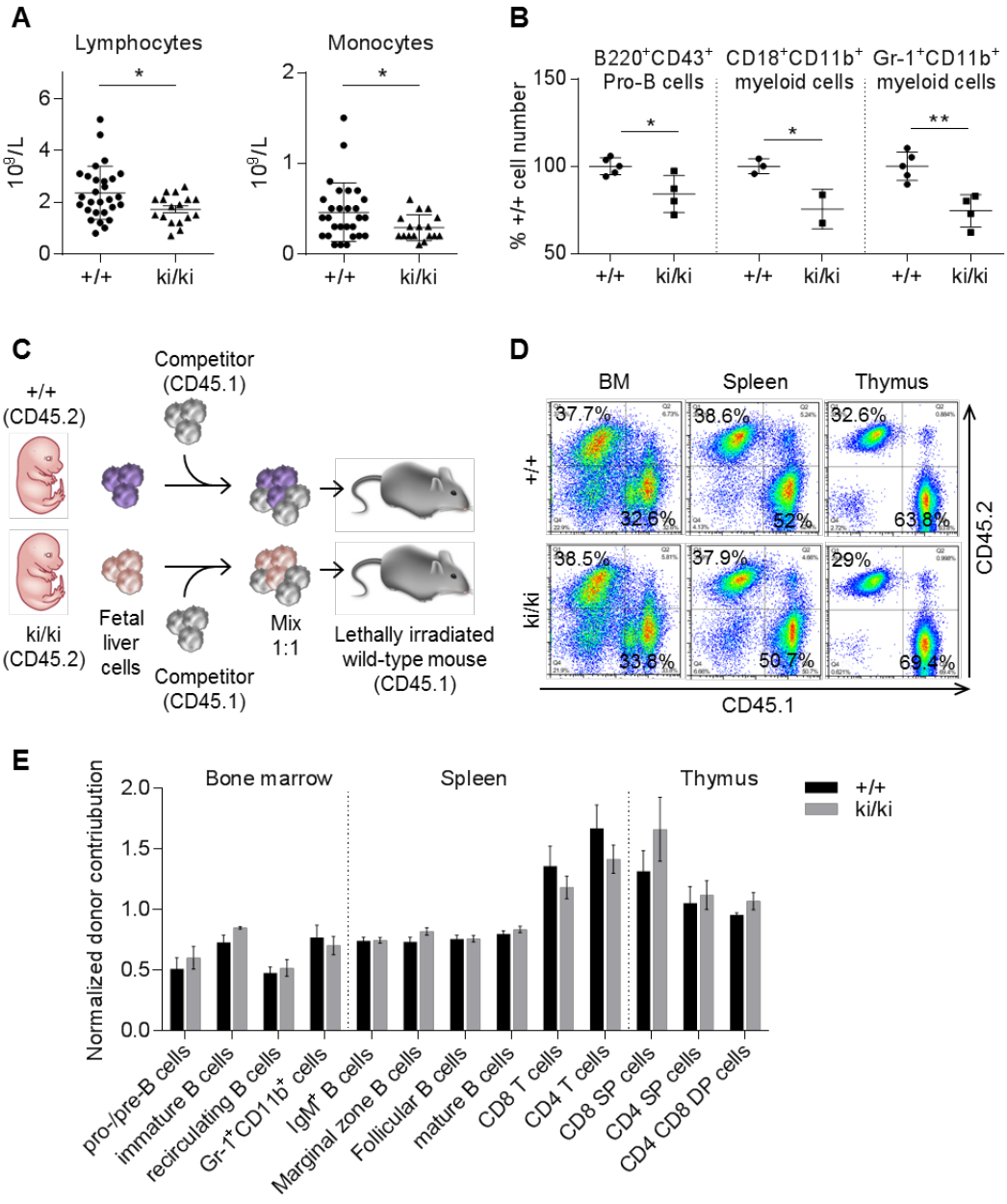

Figure 2.10. Defects in fetal hematopoiesis in DPP9$^{ki/ki}$ mice but normal development of DPP9$^{ki/ki}$ hematopoietic stem cells in competitive mixed chimeras. (**A**) Reduced number of blood lymphocytes and monocytes in newborn DPP9$^{ki/ki}$ mice. (**B**) Decreased number of Pro-B cells (B220^{+}CD43^{+}), CD18^{+}CD11b^{+} and Gr-1^{+}CD11b^{+} myeloid cells in the liver of DPP9$^{ki/ki}$ mice at E17.5 by FACS analysis. (**C**) Competitive reconstitution assay. Lethally irradiated CD45.1^{+} recipient mice were reconstituted with either CD45.2^{+} DPP9$^{ki/ki}$ or CD45.2^{+} DPP9$^{+/+}$ fetal livers, each mixed at 1:1 ratio with CD45.1^{+} wild-type fetal livers. (**D**) Representative FACS analysis of recipient bone marrow, spleen and thymus at 6 weeks after reconstitution show similar contribution of DPP9$^{ki/ki}$ and DPP9$^{+/+}$ donor cells to the reconstituted hematopoietic system. Numbers indicate relative percentage of cells gated on CD45.1 or CD45.2. (**E**) DPP9$^{ki/ki}$ and DPP9$^{+/+}$ fetal liver cells are able to reconstitute the bone marrow, spleen and thymus of mixed chimeras to a similar extend as shown by subsets of myeloid and lymphoid immune cells. SP, single positive; DP, double positive.

2.3 Discussion

DPP9 enzymatic activity controls survival of tongue muscle progenitors and its absence results in impaired tongue development, suckling defect, and neonatal lethality in mice.

Catalytically inactive DPP9 knock-in mice are neonatally lethal indicating that DPP9 enzymatic activity is essential for mouse survival (Gall et al. 2013). Despite this, the primary physiological defects responsible for their lethality and the biological function of DPP9 enzymatic activity remain unknown. In this study we analyzed the neonatal lethal phenotype of $DPP9^{ki/ki}$ mice generated by serine to alanine point mutation (S729A) in the catalytic domain of DPP9 gene, an approach identical to the one used by Gall and colleagues (Gall et al. 2013). We could show that $DPP9^{ki/ki}$ mice survive birth but die within 12 to 18 h after birth. The fact that $DPP9^{ki/ki}$ mice do not die immediately after birth together with their normal breathing and normal lung development allowed us to exclude respiratory failure as cause of their neonatal lethality. Instead, we found that $DPP9^{ki/ki}$ mice lack milk in the stomach a few hours after birth indicating abnormal feeding as the primary cause their death. Interestingly, a number of neonatal lethal mutant mice non-feeding or fasting newborns die within a window of 12-24 h after birth which is when also $DPP9^{ki/ki}$ mice die as shown by a precise identification of the timing of their death.

Complete inability of mice to feed can lead to neonatal death due to the absence of nourishment and mice survival can be rescued by manual feeding. In agreement with this, feeding of newborn $DPP9^{ki/ki}$ with cat milk rescued their survival during the entire course of the study thus confirming that feeding defects are the primary cause of their death. Video recording of dams during and after the birth revealed normal nursing by mother. Furthermore, normal fasting glucose levels in $DPP9^{ki/ki}$ mice exclude potential homeostasis defaults.

Defects in neuromuscular system, olfactory or sensory-motor neuronal pathways can also impair suckling and challenge neonatal survival (Turgeon and Meloche 2009), however, our analysis did not reveal any overt differences in $DPP9^{ki/ki}$ mice. Instead, we show that $DPP9^{ki/ki}$ mice have craniofacial defects characterized by reduced tongue size. Tongue, together with the lips and gums, form a seal against the mother's nipple and generate negative pressure to maintain nipple within the mouth and to stimulate

milk ejection (Ardran et al. 1958; Woolridge 1986). In agreement with this, DPP9$^{ki/ki}$ mice fail to attach well to mothers nipples as shown by video recording of their feeding behavior. Smaller tongue in DPP9$^{ki/ki}$ mice is accompanied by impaired formation of intrinsic distal tongue muscle but normal development of intrinsic proximal and extrinsic tongue muscles. Interestingly, the origin of tongue musculature differs depending of the type of muscle. The intrinsic distal tongue muscle is formed mainly by somatic-derived long-range migrating progenitor cells while intrinsic proximal and extrinsic tongue muscles derive from the head mesenchyme (Huang et al. 1999; Vasyutina et al. 2005). In accordance with the defect in intrinsic distal tongue muscle, DPP9$^{ki/ki}$ mice exhibited reduced number and survival of muscle progenitors deriving from occipital somites and forming distal components of the intrinsic tongue muscle. In contrast, the muscles known to derive from head mesenchyme including intrinsic proximal and extrinsic tongue muscles and masseter muscle developed normally in DPP9$^{ki/ki}$ mice. Similar tongue phenotype is observed in mice lacking genes crucial for migration of muscle progenitors. These include knockout mice of c-Met, scatter factor/hepatocyte growth factor (SF/HGF), Lbx1, Gab1 or CXCR4/Gab1 (Bladt et al. 1995; Dietrich et al. 1999; Brohmann et al. 2000; Sachs et al. 2000; Vasyutina et al. 2005). However, these knockout mice display broad defects in other hypaxial muscles deriving from migrating progenitors, such as limb or diaphragm muscles, which is not the case of DPP9$^{ki/ki}$ mice. Quantitative analysis of Lbx1 positive migratory muscle progenitors giving rise to limb muscle did not reveal any alterations in DPP9$^{ki/ki}$ mice. Furthermore, limb and diaphragm muscles were functional as demonstrated by normal movement and respiration of newborn DPP9$^{ki/ki}$ mice. One possible explanation for the tongue specific phenotype could be differences in the expression level of DPP9 enzyme or its substrate in muscle progenitors originating from occipital, cervical or limb somites. Alternatively, there might be distinct cues or survival factors which, when encountered by migratory muscle progenitors, differentially regulate their survival depending on the subpopulation of migrating muscle progenitors. This hypothesis is supported by phenotype of Lbx1 knock-out mice where not all migrating muscle progenitors are equally affected despite Lbx1 being expressed in all migrating hypaxial muscle progenitors (Brohmann et al. 2000; Gross et al. 2000).

Despite high homology and similar substrate specificity between DPP8 and DPP9, functional differences emerged in a number of studies between those enzymes (Geiss-Friedlander et al. 2009; Yao et al. 2011; Matheeussen et al. 2013). Here we show a unique role of DPP9 enzyme in the survival of migratory tongue muscle progenitors which is not compensated by DPP8 activity. Molecular mechanisms of how DPP9 enzymatic activity regulates apoptosis of tongue muscle progenitors remain largely unknown. A possible hypothesis is that DPP9 enzymatic activity regulates CXCR4-SDF-1 signaling in migrating tongue muscle progenitors. CXCR4-SDF-1 axis is important for the survival and migration of muscle progenitors (Vasyutina et al. 2005), with CXCR4 and SDF-1 being expressed by migratory muscle progenitors and their target area, respectively (Vasyutina et al. 2005). Our study excluded the possibility that DPP9 impairs migration and survival of tongue muscle progenitors by regulating CXCR4 signaling. First of all, no differences were observed in CXCR4 protein levels in $Lbx1^{+}$ tongue muscle progenitors in $DPP9^{ki/ki}$ embryos. Secondary, loss of mouse DPP9 enzymatic activity in HEK293 cells did not affect membrane localization of CXCR4 and CXCR4 signaling thus suggesting normal CXCR4 signaling in the absence of DPP9 enzymatic activity. At this stage we cannot exclude that DPP9 enzymatic activity regulates receptor binding and/or functional activity of SDF-1 by proteolytic cleavage. The N-terminal region of SDF-1 is critical for CXCR4 activation and function and the truncation of this region by DPPIV to form processed/truncated SDF-l (i.e., SDF-$l_{3–68}$) inhibits the chemotactic properties of the cell and CXCR4 signaling (Shioda et al. 1998; McQuibban et al. 2001). DPP8 shares similar substrate specificity with DPPIV and can cleave SDF-1 *in vitro* (Ajami et al. 2008). Processing of SDF-1 by DPP9 is not reported so far. Mass spectrometry could be applied to test processing of SDF-1 by DPP9 *in vitro*. Furthermore, *in situ* mass spectrometry could be used to analyze the full-length vs cleaved SDF-1 levels *ex vivo* in the first branchial arch from $DPP9^{+/+}$ and $DPP9^{ki/ki}$ embryos. It remains to be investigated whether DPP9 by processing SDF-1 regulates the survival of tongue muscle progenitors during mouse development.

An alternative hypothesis is that DPP9 enzyme modulates activity of proteins involved in apoptosis pathway. *In vitro* studies suggest the role of DPP9 enzyme in regulation of apoptosis which is cell-type or disease dependent. In line with our study, DPP8/9

inhibition results in increased spontaneous apoptosis in macrophages derived from human primary monocytes or human monocytic cell line although the underlying mechanism is not identified (Matheeussen et al. 2013). Further evidence comes from siRNA-mediated DPP9 knock down in Ewing Sarcoma tumor cell where an increased apoptosis is reported (Lu et al. 2011). This process is shown to be mediated by activation of Y1 receptor by full-length NPY_{1-36} and can be inhibited by enzymatically active DPP9. An independent group also reported processing of NPY by DPP9 *in vitro* (Bjelke et al. 2006). Therefore, DPP9 enzymatic activity could control the survival of migratory tongue muscle progenitors by cleaving NPY_{1-36} to NPY_{3-36}, and preventing the activation of Y1 receptor. Further investigations are required to validate this hypothesis since at the moment no data are available on expression of NPY or its receptors in migratory tongue muscle progenitors in mice.

The phenotype of $DPP9^{ki/ki}$ mice is similar to mice lacking c-Met or HGF/SF thus, suggesting a role for DPP9 in modulating c-Met signaling pathway. It is rather unlikely that c-Met or SF/HGF themselves are direct targets of DPP9. Muscle progenitors of c-$Met^{-/-}$ or $SF/HGF^{-/-}$ mice do not delaminate from the somites (Dietrich et al. 1999) whereas muscle progenitors in $DPP9^{ki/ki}$ mice are released and migrate towards the first branchial arch. However, mice deficient in Gab1, an important adaptor molecule of c-Met signal transduction, exhibit small tongue with reduced number of muscle progenitors accompanied by increased apoptosis similar to $DPP9^{ki/ki}$ mice (Sachs et al. 2000; Vasyutina et al. 2005). Thus, it is possible that DPP9 regulates Gab1 or related adaptor protein of a c-Met pathway. The identification of *in vivo* substrates of DPP9 will help to understand the mechanisms underlying the developmental defects in migratory tongue muscle progenitors in $DPP9^{ki/ki}$ mice.

DPP9 enzymatic activity in fetal hematopoietic stem cells is dispensable for normal hematopoiesis

We studied the immune-related phenotype of $DPP9^{ki/ki}$ mice because of i) DPP9 protein and mRNA expression and the reported DPP8/9 enzymatic activity in the immune cells (Ajami et al. 2004; Maes et al. 2007; Yu et al. 2009; Chowdhury et al. 2013) and this study, ii) the immunosuppressive activity of DPP8/9 dual inhibitor in *in vitro* studies (Lankas et al. 2005; Reinhold et al. 2009) and iii) controversial data on

the immune-related toxicity of DPP8/9 dual inhibitors (Lankas et al. 2005; Wu et al. 2009). Furthermore, pharmacological studies with DPP8/9 dual inhibitors could not address the respective contribution of DPP8 and DPP9 inhibition to *in vivo* toxicity. Thus, $DPP9^{ki/ki}$ mice enabled us to mimic the effect of a selective DPP9 inhibitor which is not yet available. $DPP9^{ki/ki}$ mice showed reduced number of lymphoid and myeloid cells in fetal liver and postnatal blood. However, their hematopoietic stem cells were fully competent in reconstituting the immune system of lethally irradiated recipients, implying a dispensable role of DPP9 enzyme in normal hematopoiesis. We cannot rule out DPP9 enzymatic activity in non-hematopoietic cells which might regulate hematopoiesis and notably, this might be the cause of the hematopoiesis defect shown in $DPP9^{ki/ki}$ mice. Reconstitution of lethally irradiated conditional DPP9 enzyme-inactive mice with wild-type fetal liver cells could be applied to elucidate the role of non-hematopoietic cell-derived DPP9 activity in hematopoiesis. Furthermore, although DPP9 enzyme is not essential for normal hematopoiesis we cannot exclude the role of DPP9 enzyme under certain circumstances, for example, in the presence of antigens or in a disease setting. Thus, further investigation is required to clarify the contribution of DPP9 activity in hematopoiesis and immune responses under diverse physiological conditions.

2.4 Conclusions

Dipeptidyl peptidase 9 (DPP9), an intracellular N-terminal post-proline-cleaving enzyme, is implicated in cell behavior and immune responses but its physiological function remains largely unknown. Here we investigated *in vivo* role of DPP9 enzyme by characterizing DPP9 knock-in mice expressing a catalytically inactive S729A mutant of DPP9 ($DPP9^{ki/ki}$ mice). We show that impaired suckling response is a primary cause of perinatal lethality of $DPP9^{ki/ki}$ mice which die within 12-18 h after birth and can be rescued by manual feeding. Suckling defect is a result of microglossia characterized by defects in the formation of intrinsic distal tongue muscle known to derive from migratory muscle progenitors while intrinsic proximal and extrinsic tongue muscles deriving from head mesenchyme develop normally in $DPP9^{ki/ki}$ mice. Smaller tongue size of $DPP9^{ki/ki}$ mice correlates with reduced number and impaired

survival of migratory tongue muscle progenitors. CXCR4 mediated survival and migration of muscle progenitors is not impaired in the absence of DPP9 enzymatic activity however, an effect of DPP9 enzyme on SDF-1, ligand of CXCR4, cannot be excluded. In addition, we show that $DPP9^{ki/ki}$ mice exhibit impaired fetal hematopoiesis however their hematopoietic stem cells are fully competent in reconstitution of myeloid and lymphoid lineages in lethally irradiated mice. Taken together, our studies revealed for the first time that DPP9 enzyme controls survival of migratory tongue muscle progenitors and its absence in mice leads to impaired tongue development, suckling defect and neonatal lethality but DPP9 enzymatic activity in hematopoietic cells is dispensable for normal hematopoiesis.

2.5 Materials and methods

Generation of DPP9 and DPP8 knock-in mice

Mice with a targeted DPP9 locus were generated by homologous recombination in ES cells. The targeting vector was constructed using C57BL/6 mouse genomic DNA. The TCC → GCC mutation in nucleotide 97 – 99 of exon 18 of the DPP9 gene (NCBI Reference Sequence: NM_172624.3) was introduced by overlapping polymerase chain reaction. Mutated exon 18 was subcloned in multiple cloning site of pRay-MCS1-2lox-2frt vector, surrounded by two LoxP sites. As long homology arm, a 4 kb 5' fragment encompassing end of intron 15, exons 16 and 17 was amplified and further cloned upstream of the 5' LoxP site. Short homology arm, a 1.9 kb 3' fragment containing introns 19 and 20 was amplified and subcloned down stream of second FRT site in cloning vector. The DPP9 targeting vector contained a neomycin resistance gene (neo^R) flanked by two FRT sites. NotI linearized targeting vector was electroporated into C57BL/6 ES cells. Neomycin resistant clones were isolated and analyzed for homologous recombination by nested PCR using the primer pairs TCCTCGTGCTTTACGGTA – TGCCTGCTATAAATCCATC and CTATCGCCTTCTTGACGA – CCACCCAAACCTCAGGTC. For Southern blot, 4 µg of genomic DNA was digested with 25 units of Sac I, separated on a 0.8% agarose gel followed by vacuum blotting with 20× SSC on nylon membrane. Hybridization with the ^{32}P ([$\alpha^{32}P$]dCTP, Hartmann Analytic)-labeled DNA probe (Rediprime II, GE

Healthcare) was performed in Perfect Plus Hybridization buffer (Sigma) at 65°C overnight followed by image analysis using a FLA-5000 imaging system (Fujifilm). Targeted C57BL/6 ES clones were injected into Balb/C host blastocysts and transferred into pseudopregnant CB6F1 foster mothers. Male chimeric mice were crossed with wild type C57BL/6 mice to produce F1 animals. Black offspring indicated the germline transmission of the targeted ES cells. Males carrying modified DPP9 gene were mated with female mice expressing the Flp recombinase to remove the neomycin resistance cassette. The Flp recombinase was removed in a subsequent breeding step with wild-type mice. DPP9 knock-in heterozygous ($DPP9^{ki/+}$) mice were mated to obtain DPP9 knock-in homozygous ($DPP9^{ki/ki}$) mice. Genotyping was performed by PCR on tail DNA using the following primers: TATGATGGCAGTGATGATC and CTTAGACGCCAAGTAGTATTTA, with expected bands sizes of 143 bp for wild-type and 191 bp for transgenic allele. DPP8 knock-in mice were generated using similar strategy with a S749A mutation in DPP8 protein.

Synthesis of fluorphosphonate (FP)-biotin

Bionylated PEG linker azide and biotin-PEG(3+4)-N_3 were purchased from Iris Biotech GmbH and all other reagents and solvents were purchased from Sigma. An FP-alkyne intermediate was synthesized as described previously (Gillet et al. 2008) and fused to biotin-PEG(3+4)-N_3 by a copper catalyzed cycloaddition (also referred to as click-chemistry) to obtain the FP-biotin. A solution of FP-alkyne intermediate (0.075 mmol) in DMSO (750 µl) in 10 ml round bottom flask was added a solution of biotin-PEG(3+4)-N_3 (36 mg, 0.050 mmol) in DMSO (500 µl). Separately, copper (I) bromide (7.17 mg, 0.050 mmol) was dissolved in MeCN (722 µl) and added to Tris[(1-benzyl-1H-1, 2, 3-triazol-4-yl)methyl]amine (26.5 mg, 0.050 mmol). The resulting clear solution was introduced to the substrate solution above. The reaction was swirled at 23°C for 16 h. MeCN was evaporated, and the residue was diluted with TBME (10 ml). The resulting suspension was centrifuged and the precipitate was washed with TBME, suspended in MeCN, centrifuged, and the supernatant was collected. This step was repeated and the combined MeCN supernatant was evaporated. The residue was taken up in water (ca. 10 ml) and extracted with dichloromethane (10 ml × 5). The

combined dichloromethane phase was dried over Na_2SO_4, filtered and evaporated. The residue was again taken up in water (10 ml), which was washed with EtOAc (10 ml × 2), then extracted with dichloromethane (10 ml × 5). The combined dichloromethane phase was dried over Na_2SO_4, filtered, evaporated to give FP-biotin (15.1 mg, 0.014 mmol, 28.6 % yield) as a yellow film. ^{1}H-NMR: (400MHz, d6-DMSO) δ-NMP: (400MHζ, UPLC-MS: Acquity HSS T3 1.8 µm 2.1 × 50 mm at 50°C, solvents A1 = water + 0.1 % HCOOH, B1 = MeCN + 0.1 % HCOOH, 5 -> 90 % B1 in 2.5 min, Rt = 0.62 min, SQ pos [M+H$^+$] 1003.04, [M+Na$^+$] 1025.03, SQ neg [M+HCOO$^-$] 1047.13 H-NMR: d6-DMSO, consistent with the expected structure.

Recombinant protein expression and purification

Full-length human DPP8 cDNA was subcloned into pFastBac1 vector (Life Technologies) with His and V5 tag and expressed in insect Sf9 cells using the Bac-to-Bac baclovirus expression system (Life Technologies) followed by affinity purification with His tag using Talon Cellthru metal affinity column (Clontech). Full-length human DPP9 and PEP cDNA were subcloned into pPICZα-His vector (Life technologies) with His tag and expressed in *Pichia pastoris* X-33 cells (Life technologies) followed by affinity purification with His tag using Ni-NTA beads (Qiagen).

Activity-based probe (ABP) pull down assay

Half of the snap frozen brain (~50 mg) from new born mice was homogenized in 300 µl of Lysis buffer (100 mM Tris-HCl pH 7.3, 100 mM NaCl, 5% glycerol, 1.5 mM $MgCl_2$, 1 mM DTT and 0.8% NP-40) containing 250U Benzonase (Sigma) with matrix D beads using FastPrep-24 (MP Biomedicals). Lysates were centrifuged at 14,000 rpm, 4°C for 20 min and 2 mg of lysates or 30 nM of human DPP8 and DPP9 recombinant proteins were incubated with 10 µM of FP-biotin for 1 h at RT. Reaction was quenched with 0.25% SDS and samples were diluted to 1 ml with wash buffer (100 mM Tris-HCl pH 7.3, 100 mM NaCl, 5% glycerol, 1.5 mM $MgCl_2$, 1 mM DTT and 0.25% SDS) followed by incubation with 200 µl of high capacity streptavidin beads (Thermo Sci.) for 1 h at RT. Samples were centrifuged at 300 × g for 5 min to remove supernatant and washed twice by gravity flow. Proteins bound to FP-biotin were eluted with elution buffer (100 mM phosphate buffer pH 10.2, 2.8% SDS, 18% glycerol, 160 mM DTT, 30 mM biotin, 0.02% Bromophenol blue) at 90°C for 10 min

at 700 rpm Thermomixer (Eppendorf). Eluted fractions and human DPP9, DPP8 and PEP recombinant proteins were loaded on 4-12% Bis/Tris gel (Life Technologies) and western blot was performed using rabbit anti-DPP8, DPP9 and PEP antibodies (all from Abcam).

Transfection

Plasmids containing the full-length of mouse DPP9 and DPP8 cDNA were purchased from Biocat. Mouse CXCR4 was cloned from RAW264.7 cDNA library and subcloned into pcDNA3.1 vector for expression of C-terminal V5-His tagged CXCR4 using pcDNA 3.1D TOPO expression kit (Life Technologies). Plasmid expressing enzyme-inactive S729A mutant of mouse DPP9 (mutDPP9) was generated using primers for site-directed mutagenesis. HEK293 cells were obtained from ATCC and grown in DMEM supplemented with 10% fetal calf serum, 1 mM sodium pyruvate, 1 mM L-glutamine and 1% penicillin/streptomycin. For the transient transfection, HEK293 cells were transfected with 3 µg of DPP8 or DPP9 plasmids using XtremeGene (Roche) according to manufacturer's instructions. To generate HEK293 cells stably expressing CXCR4 with a C-terminal V5-His tag (CXCR4 stable cell line), cells were transfected with 1 µg of plasmids using XtremeGene (Roche) according to manufacturer's instructions and selected for G418 resistance. Positive clones were selected on the basis of V5 epitope expression using confocal microscopy. Cells were further transiently transfected with mouse wile-type DPP9 plasmid or mutDPP9 plasmid.

***In situ* hybridization**

Decapitated newborn mice and E10.75 embryos were fixed in 10% buffered formalin for 48 h or 24 h, respectively at RT. Transfected HEK293 cells were fixed in 10% buffered formalin overnight at 4°C. Tissues and cell pellets were processed for embedding in paraffin using standard procedures. 3 µm sections were deparaffinized in xylene and rehydrated through graded ethanol series. RNAscope 2.0 HD RED kit and probes (Advanced Cell Diagnostics) were used according to the manufacturer's instructions with DapB as a negative control. Digital images were obtained with a ScanScope XT system (Leica).

Histology, immunohistochemistry and quantitative image analysis

Hematoxylin and eosin (H&E) staining

Decapitated newborn mice, embryos (E12.5-18.5) or organs (P1 brains) were fixed in 10% buffered formalin for 48 h at RT and embedded in paraffin using standard procedures. 3 µm sections were deparaffinized in xylene and rehydrated through graded ethanol series. Sections were stained with H&E using standard protocol.

Chromogenic DPP9 staining:

Decapitated newborn mice were fixed in 10% buffered formalin for 48 h at RT. Transfected HEK293 cells and human blood $CD45^+$ cells were fixed in 10% buffered formalin for overnight at 4°C. Tissues and cell pellets were processed for embedding in paraffin using standard procedures. 3 µm sections were deparaffinized in xylene and rehydrated through graded ethanol series. Endogenous peroxidase activity was quenched and sections were incubated with rabbit anti-DPP9 antibody (Abcam) followed by chromogenic detection with Histofine Simple Stain system (Nichirai Biosciences) and DAB (Sigma). Normal rabbit IgG (Cell Signaling) was used as a negative control. Digital images were obtained with a ScanScope XT system (Leica).

Immunofluorescence staining:

E10.75 embryos were fixed with 4% paraformaldehyde in PBS for 2 h, cryopreserved in 30% sucrose overnight at 4°C, and OCT embedded. 12 µm-consecutive sections were collected throughout the hypoglossal cord and forelimb. The following antibodies were used: guinea pig anti-mouse Lbx1 (Muller et al. 2002); rabbit anti-cleaved caspase3 (Cell Signaling); rabbit anti-CXCR4 (Abcam); rabbit anti-DPP9 (Abcam) and secondary antibodies conjugated with Alexa Fluor 488 or 594 (Life Technologies). CXCR4 was visualized by Cy3-TSA Fluorescence System (PerkinElmer Life Sciences). $Lbx1^+$ or cleaved caspase 3^+ area was reconstructed in consecutive sections from hypoglossal cord and analyzed as % of wild type littermate signal. $Lbx1^+$ or cleaved caspase 3^+ area was quantified in 4 representative sections from forelimb of each embryo and analyzed as % of wild type littermate signal. For immunocytochemistry, transfected CXCR4 stable cell line was fixed with 4% paraformaldehyde in PBS for 10 min, permeabilized with 0.25% Triton X-100 in PBS for 5 min and blocked with 10% horse serum in PBS for 1 h at RT. Cells were incubated with rabbit anti-DPP9 antibody (Abcam) and mouse anti-V5 antibody (Life

Technologies) for 2 h and secondary antibodies conjugated with Alexa Fluor 488 or 594 (Life Technologies) for 1 h at RT. LSM700 confocal microscope (Zeiss), Axio Observer Z1 microscope (Zeiss) and AxioVision software (Zeiss) were used for image analysis. n=3 to 7 per group.

Whole mount neurofilament staining:

E10.5 embryos were fixed in 4% paraformaldehyde overnight at 4°C. Endogenous peroxidase was blocked by incubating the embryos overnight at 4°C in wash buffer (1% Triton X-100 and 10% fetal calf serum in PBS) containing 0.1% hydrogen peroxide. Embryos were washed 3 times for 60 min in wash buffer and incubated with anti-neurofilament antibody (2H3, Developmental Studies Hybridoma Bank) diluted 1:1 in wash buffer for 3 days at 4°C. Embryos were washed 3 times for 60 min in wash buffer and incubated with peroxidase-conjugated goat anti-mouse IgG (Jackson ImmunoResearch) diluted 1:100 in wash buffer for overnight at 4°C. Embryos were incubated in 0.7 mg/ml DAB (Sigma) in PBS twice for 10 min and the peroxidase reaction was visualized by addition of hydrogen peroxide (Sigma) to 0.02%. When the nerves were visible (~5 min), reaction was stopped by rinsing the embryos in PBS. Embryos were photographed on Z16 Apo A macroscope (Leica). n=7 per group.

Cytochrome oxidase staining:

Newborn mice were perfused with 4% paraformaldehyde in PBS. Brains were dissected and post-fixed overnight at 4°C with 4% paraformaldehyde in PBS. Agarose-embedded brains were cut into 70 µm sections with Vibratome (Leica). Sections were incubated in a solution containing 2.4 g of sucrose, 24 mg of cytochrome oxidase (Sigma) and 20 mg of DAB (Sigma) in 30 ml of PBS at 37°C in the dark until a golden brown staining was observed, followed by incubation in 100% ethanol and mounting onto slide with Aqua-Poly/Mount (Polysciences). Digital images were obtained with Axio Observer Z1 microscope (Zeiss) n=4 per group.

Motor neuron analysis:

Trigeminal, facial or hypoglossal motor nuclei were manually counted on H&E-stained brainstem sections from new born mice covering the largest area of respective nuclei.

Neuromuscular junction staining:

Masseter and tongue muscles were dissected from decapitated newborn mice, fixed with 1% paraformaldehyde in PBS for 10 min at RT, and teased into bundles. Bundles

were permeabilized with 1% Triton X-100 in PBS for 10 min, incubated with 0.1M glycine in PBS, and blocked with blocking buffer (0.1% Triton X-100 and 1% BSA in PBS) for 30 min. Bundles were incubated with rabbit anti-neurofilament antibody (Sigma) in blocking buffer for overnight at 4°C, washed three times for 60 min in 1% BSA in PBS, and incubated with α-BTX conjugated with Alexa 488 (Life Technologies) and Alexa 594 conjugated chicken anti-rabbit IgG (Life Technologies) for 45 min in 1% BSA in PBS. Bundles were washed with 1% BSA in PBS for 2 h, rinsed with PBS, mounted onto slides with FluorSave (Millipore), and imaged with LSM700 confocal microscope (Zeiss). n=3 to5 per group.

Manual feeding

Newborn mice were fed with babycat milk (protein 33%, fat 39%; Royal Canin) dissolved at 1:6 in water (36°C) (Kutsuwada et al. 1996). Mice, separated from mother after birth and kept in moist chamber (Scantainer) at 33~34°C, were grasped by the skin on the back of the neck, and fed with milk slowly dosed into their oral cavity (Butchbach et al. 2007). 5 µl of milk was given every 2 h for 24 h and the surviving pups were euthanized at the end of the experiment.

Suckling behavior

Suckling behavior assay was adapted from previous study (Liu et al. 2015). Mother mouse was anesthetized and placed on warm pad (33~34°C). Pups were supported 5 mm from mother's nipple for 2 min with unrestricted movement to the nipple. Nipple localization, rhythmic jaw movement and nipple's attachment were assessed twice. The trail was regarded as 'succeed' when the pup accomplished it at least once, and counted as 'fail' when the pup failed twice.

Blood glucose measurement

Newborn mice were separated from mother after birth and kept in moist chamber (Scantainer) for 3 h. Pups were sacrificed by decapitation and blood glucose levels were measured using an Accu-Chek glucometer (Roche).

Body weight and food intake measurement

Mice were housed individually and their the body weight and food consumption was monitored weekly, starting at the age of 5 weeks and continuing until the age of 25

weeks. All measurements were taken at the same time in the morning. n=16 to 19 per group.

cAMP radiometric assay

Untransfected or transfected CXCR4 stable cell line were grown as confluent monolayers in 48-well tissue culture dishes and incubated with [^{3}H]adenine (Amersham, 100 MBq/ml) and/or pertussis toxin (PTX, Sigma, final concentration 0.4 µg/ml) for 4 h in serum-free DMEM supplemented with 1% penicillin/streptomycin. After removing of the medium, cells were washed with Assay medium [20mM HEPES (Life Technologies) and 1g/L fatty acid free BSA (Calbiochem) in HBSS (Life Technologies)], and subsequently supplemented with 100 µl of Assay medium containing 1 mM IBMX (Fluka) to block phosphodiesterases. Into the appropriate wells, forskolin (Sigma, final concentration 40 µM) and/or human recombinant SDF-1α (R&D Systems, final concentration 50 ng/ml) was added. After the 20 min incubation at 37°C, the medium was replaced by 100 µl of ice-cold 5% trichloroacetic acid (TCA; Fluka), supplemented with 100 µl of ice-cold carrier solution containing 0.1 mM ATP (Boehringer), and 0.1 mM cAMP (Boehringer) in 5% TCA. Labeled cAMP was separated from free adenine and ATP using a batch column chromatography as previously described (Salomon 1979). n=3 per group.

Human blood immune cells analysis

Isolation:

Peripheral blood was collected from healthy donors and $CD4^+$, $CD8^+$, $CD19^+$, $CD14^+$, $CD15^+$, $CD56^+$, and $CD45^+$ cells were isolated using respective Whole Blood MicroBeads (Miltenyi Biotec) according to the manufacturer's instructions. Plasmacytoid dendritic cells (pDCs) were enriched from PBMCs by Easysep Human pDC Enrichment kit and Robosep instrument (Stemcell technologies) according to the manufacturer's instruction. n=5 per group.

Real time qRT-PCR:

RNA was isolated using an RNeasy Micro kit (Qiagen) according to the manufacturer's instructions. Quantitative real-time PCR was performed for DPP9 and DPP8 using Taqman Universal Master Mix and the ABI Prism 7900 HT Sequence Detection System (Applied Biosystems). n=5 per group.

Peripheral blood analysis

Newborn mice were decapitated and bloods were collected in EDTA tubes. Differential blood counts were obtained using an automated ADVIA 2120i Hematology System (Siemens).

Competitive reconstitution analysis

E17.5 fetal liver cells (2.5 x 10^6 cells) from $DPP9^{+/+}$ or $DPP9^{ki/ki}$ embryos (CD45.2) were mixed with the equal number of E17.5 wild-type competitor fetal liver cells (CD45.1) and injected intravenously into wild-type recipient mice (CD45.1) irradiated at a dose of 9 Gy (Gammacell 40, Best Theratronics). 6 weeks after the reconstitution, bone marrow cells, splenocytes and thymocytes from recipient mice were analyzed using flow cytometry. For contribution of $DPP9^{+/+}$ fetal liver cells and $DPP9^{ki/ki}$ fetal liver cells to multilineage reconstitution of recipients, pro/pre-B cells ($CD19^+c\text{-}kit^+$), immature B cells (IgM^+B220^{low}), recirculating B cells (IgM^+B220^{high}) and Gr-1^+CD11b^+ cells in bone marrow; IgM^+ B cells (IgM^+B220^+), marginal zone B cells ($CD19^+CD21^{high}$), follicular B cells ($CD19^+CD21^+CD23^{high}$), mature B cells ($CD19^+CD93^-$), CD8 T cells (TCR^+CD8^+) and CD4 T cells (TCR^+CD4^+) in spleen; CD8 SP cells ($CD4^-CD8^+$), CD4 SP cells ($CD4^+CD8^-$) and CD4 CD8 DP cells ($CD4^+CD8^+$) in thymus were analyzed for CD45.1 or CD45.2. The % $CD45.2^+$ cells/% $CD45.1^+$ cells ratio was calculated for each subpopulation of cells in individual animals. This value was divided by the % $CD45.2^+$ cells/% $CD45.1^+$ cells ratio of total cells in the organ of individual animals to account for the variation of reconstitution efficiency in each animal. n=3 per group.

Flow cytometry

Single-cell suspensions of bone marrow, spleen, thymus, and liver were prepared by mechanical disruption, stained with appropriate reagents, and analyzed using a FACSCalibur (Becton Dickinson) or CyAn ADP 9 color Analyzer (Beckman Coulter) and FlowJo software (FlowJo). Anti-CD19-PE or -PECy7 (1D3), anti-B220-PE or -FITC (RA3-6B2), anti-c-kit-APC (2B8), anti-CD11b-PE (M1/70), anti-CD23-PE (B3B4), anti-CD4-PECy7 (GK1.5), anti-TCR-PE (H57), anti-CD18-PE (C71/16) and APC conjugated streptavidin were purchased from BD Biosciences. Anti-Gr-1-Biotin (RB6-8C5) was purchased from PharMingen. PE-conjugated streptavidin was

purchased from Southern Biotech. Anti-CD43-PECy7 (1B11), anti-CD11b -Pacific Blue (M1/70) and anti-Gr-1-APC (RB6-8C5) were purchased from Biolegend. Anti-IgM-APC (M41), anti-CD19-APC (1D3), anti-CD93-Biotin (PB493), anti-CD21-APC (7G6), anti-CD8-APC (53-6.7), anti-CD45.1-FITC (A20) and anti-CD45.2-APC (104.2.1) were produced and labeled in laboratory of Prof. A. Rolink according to standard techniques.

Statistical analysis

The results are presented as mean ± SEM. Unpaired t test was used for the comparisons between two groups. *: $p< 0.05$; **: $p <0.01$; ***: $p <0.001$.

2.6 References

Abbott CA, Yu DM, Woollatt E, Sutherland GR, McCaughan GW, Gorrell MD. 2000. Cloning, expression and chromosomal localization of a novel human dipeptidyl peptidase (DPP) IV homolog, DPP8. *European journal of biochemistry / FEBS* **267**: 6140-6150.

Ajami K, Abbott CA, McCaughan GW, Gorrell MD. 2004. Dipeptidyl peptidase 9 has two forms, a broad tissue distribution, cytoplasmic localization and DPIV-like peptidase activity. *Biochimica et biophysica acta* **1679**: 18-28.

Ajami K, Pitman MR, Wilson CH, Park J, Menz RI, Starr AE, Cox JH, Abbott CA, Overall CM, Gorrell MD. 2008. Stromal cell-derived factors 1alpha and 1beta, inflammatory protein-10 and interferon-inducible T cell chemo-attractant are novel substrates of dipeptidyl peptidase 8. *FEBS letters* **582**: 819-825.

Ardran GM, Kemp FH, Lind J. 1958. A cineradiographic study of bottle feeding. *The British journal of radiology* **31**: 11-22.

Bank U, Heimburg A, Wohlfarth A, Koch G, Nordhoff K, Julius H, Helmuth M, Breyer D, Reinhold D, Tager M et al. 2011. Outside or inside: role of the subcellular localization of DP4-like enzymes for substrate conversion and inhibitor effects. *Biological chemistry* **392**: 169-187.

Bjelke JR, Christensen J, Nielsen PF, Branner S, Kanstrup AB, Wagtmann N, Rasmussen HB. 2006. Dipeptidyl peptidases 8 and 9: specificity and molecular characterization compared with dipeptidyl peptidase IV. *The Biochemical journal* **396**: 391-399.

Bladt F, Riethmacher D, Isenmann S, Aguzzi A, Birchmeier C. 1995. Essential role for the c-met receptor in the migration of myogenic precursor cells into the limb bud. *Nature* **376**: 768-771.

Blass EM, Teicher MH. 1980. Suckling. *Science* **210**: 15-22.

Brohmann H, Jagla K, Birchmeier C. 2000. The role of Lbx1 in migration of muscle precursor cells. *Development* **127**: 437-445.

Butchbach ME, Edwards JD, Schussler KR, Burghes AH. 2007. A novel method for oral delivery of drug compounds to the neonatal SMNDelta7 mouse model of spinal muscular atrophy. *Journal of neuroscience methods* **161**: 285-290.

Carim-Todd L, Escarceller M, Estivill X, Sumoy L. 2000. Cloning of the novel gene TM6SF1 reveals conservation of clusters of paralogous genes between human chromosomes 15q24-->q26 and 19p13.3-->p12. *Cytogenetics and cell genetics* **90**: 255-260.

Chevallier A, Kieny M, Mauger A. 1977. Limb-somite relationship: origin of the limb musculature. *Journal of embryology and experimental morphology* **41**: 245-258.

Chowdhury S, Chen Y, Yao TW, Ajami K, Wang XM, Popov Y, Schuppan D, Bertolino P, McCaughan GW, Yu DM et al. 2013. Regulation of dipeptidyl

peptidase 8 and 9 expression in activated lymphocytes and injured liver. *World journal of gastroenterology : WJG* **19**: 2883-2893.

Christ B, Jacob HJ, Jacob M. 1977. Experimental analysis of the origin of the wing musculature in avian embryos. *Anatomy and embryology* **150**: 171-186.

Christ B, Ordahl CP. 1995. Early stages of chick somite development. *Anatomy and embryology* **191**: 381-396.

Dietrich S, Abou-Rebyeh F, Brohmann H, Bladt F, Sonnenberg-Riethmacher E, Yamaai T, Lumsden A, Brand-Saberi B, Birchmeier C. 1999. The role of SF/HGF and c-Met in the development of skeletal muscle. *Development* **126**: 1621-1629.

Eckardt S, McLaughlin KJ. 2008. Transplantation of chimeric fetal liver to study hematopoiesis. *Methods in molecular biology* **430**: 195-211.

Gall MG, Chen Y, Vieira de Ribeiro AJ, Zhang H, Bailey CG, Spielman DS, Yu DM, Gorrell MD. 2013. Targeted inactivation of dipeptidyl peptidase 9 enzymatic activity causes mouse neonate lethality. *PloS one* **8**: e78378.

Geiss-Friedlander R, Parmentier N, Moller U, Urlaub H, Van den Eynde BJ, Melchior F. 2009. The cytoplasmic peptidase DPP9 is rate-limiting for degradation of proline-containing peptides. *The Journal of biological chemistry* **284**: 27211-27219.

Gillet LC, Namoto K, Ruchti A, Hoving S, Boesch D, Inverardi B, Mueller D, Coulot M, Schindler P, Schweigler P et al. 2008. In-cell selectivity profiling of serine protease inhibitors by activity-based proteomics. *Molecular & cellular proteomics : MCP* **7**: 1241-1253.

Gross MK, Moran-Rivard L, Velasquez T, Nakatsu MN, Jagla K, Goulding M. 2000. Lbx1 is required for muscle precursor migration along a lateral pathway into the limb. *Development* **127**: 413-424.

Huang R, Zhi Q, Izpisua-Belmonte JC, Christ B, Patel K. 1999. Origin and development of the avian tongue muscles. *Anatomy and embryology* **200**: 137-152.

Kutsuwada T, Sakimura K, Manabe T, Takayama C, Katakura N, Kushiya E, Natsume R, Watanabe M, Inoue Y, Yagi T et al. 1996. Impairment of suckling response, trigeminal neuronal pattern formation, and hippocampal LTD in NMDA receptor epsilon 2 subunit mutant mice. *Neuron* **16**: 333-344.

Lankas GR, Leiting B, Roy RS, Eiermann GJ, Beconi MG, Biftu T, Chan CC, Edmondson S, Feeney WP, He H et al. 2005. Dipeptidyl peptidase IV inhibition for the treatment of type 2 diabetes: potential importance of selectivity over dipeptidyl peptidases 8 and 9. *Diabetes* **54**: 2988-2994.

Liu N, Zhang Z, Wu H, Jiang Y, Meng L, Xiong J, Zhao Z, Zhou X, Li J, Li H et al. 2015. Recognition of H3K9 methylation by GLP is required for efficient establishment of H3K9 methylation, rapid target gene repression, and mouse viability. *Genes & development* **29**: 379-393.

Liu Y, Patricelli MP, Cravatt BF. 1999. Activity-based protein profiling: the serine hydrolases. *Proceedings of the National Academy of Sciences of the United States of America* **96**: 14694-14699.

Lu C, Tilan JU, Everhart L, Czarnecka M, Soldin SJ, Mendu DR, Jeha D, Hanafy J, Lee CK, Sun J et al. 2011. Dipeptidyl peptidases as survival factors in Ewing sarcoma family of tumors: implications for tumor biology and therapy. *The Journal of biological chemistry* **286**: 27494-27505.

Maes MB, Dubois V, Brandt I, Lambeir AM, Van der Veken P, Augustyns K, Cheng JD, Chen X, Scharpe S, De Meester I. 2007. Dipeptidyl peptidase 8/9-like activity in human leukocytes. *Journal of leukocyte biology* **81**: 1252-1257.

Matheeussen V, Waumans Y, Martinet W, Van Goethem S, Van der Veken P, Scharpe S, Augustyns K, De Meyer GR, De Meester I. 2013. Dipeptidyl peptidases in atherosclerosis: expression and role in macrophage differentiation, activation and apoptosis. *Basic research in cardiology* **108**: 350.

McQuibban GA, Butler GS, Gong JH, Bendall L, Power C, Clark-Lewis I, Overall CM. 2001. Matrix metalloproteinase activity inactivates the CXC chemokine stromal cell-derived factor-1. *The Journal of biological chemistry* **276**: 43503-43508.

Muller T, Brohmann H, Pierani A, Heppenstall PA, Lewin GR, Jessell TM, Birchmeier C. 2002. The homeodomain factor lbx1 distinguishes two major programs of neuronal differentiation in the dorsal spinal cord. *Neuron* **34**: 551-562.

Olsen C, Wagtmann N. 2002. Identification and characterization of human DPP9, a novel homologue of dipeptidyl peptidase IV. *Gene* **299**: 185-193.

Reinhold D, Goihl A, Wrenger S, Reinhold A, Kühlmann UC, Faust J, Neubert K, Thielitz A, Brocke S, Täger M et al. 2009. Role of dipeptidyl peptidase IV (DP IV)-like enzymes in T lymphocyte activation: investigations in DP IV/CD26-knockout mice. *Clinical Chemistry and Laboratory Medicine* **47**.

Sachs M, Brohmann H, Zechner D, Muller T, Hulsken J, Walther I, Schaeper U, Birchmeier C, Birchmeier W. 2000. Essential role of Gab1 for signaling by the c-Met receptor in vivo. *The Journal of cell biology* **150**: 1375-1384.

Salomon Y. 1979. Adenylate cyclase assay. *Advances in cyclic nucleotide research* **10**: 35-55.

Shioda T, Kato H, Ohnishi Y, Tashiro K, Ikegawa M, Nakayama EE, Hu H, Kato A, Sakai Y, Liu H et al. 1998. Anti-HIV-1 and chemotactic activities of human stromal cell-derived factor 1alpha (SDF-1alpha) and SDF-1beta are abolished by CD26/dipeptidyl peptidase IV-mediated cleavage. *Proceedings of the National Academy of Sciences of the United States of America* **95**: 6331-6336.

Tang HK, Tang HY, Hsu SC, Chu YR, Chien CH, Shu CH, Chen X. 2009. Biochemical properties and expression profile of human prolyl dipeptidase DPP9. *Archives of biochemistry and biophysics* **485**: 120-127.

Turgeon B, Meloche S. 2009. Interpreting neonatal lethal phenotypes in mouse mutants: insights into gene function and human diseases. *Physiological reviews* **89**: 1-26.

Vasyutina E, Stebler J, Brand-Saberi B, Schulz S, Raz E, Birchmeier C. 2005. CXCR4 and Gab1 cooperate to control the development of migrating muscle progenitor cells. *Genes & development* **19**: 2187-2198.

Wilson CH, Indarto D, Doucet A, Pogson LD, Pitman MR, McNicholas K, Menz RI, Overall CM, Abbott CA. 2013. Identifying natural substrates for dipeptidyl peptidases 8 and 9 using terminal amine isotopic labeling of substrates (TAILS) reveals in vivo roles in cellular homeostasis and energy metabolism. *The Journal of biological chemistry* **288**: 13936-13949.

Woolridge MW. 1986. The 'anatomy' of infant sucking. *Midwifery* **2**: 164-171.

Wu JJ, Tang HK, Yeh TK, Chen CM, Shy HS, Chu YR, Chien CH, Tsai TY, Huang YC, Huang YL et al. 2009. Biochemistry, pharmacokinetics, and toxicology of a potent and selective DPP8/9 inhibitor. *Biochemical pharmacology* **78**: 203-210.

Yao TW, Kim WS, Yu DM, Sharbeen G, McCaughan GW, Choi KY, Xia P, Gorrell MD. 2011. A novel role of dipeptidyl peptidase 9 in epidermal growth factor signaling. *Molecular cancer research : MCR* **9**: 948-959.

Yu DM, Ajami K, Gall MG, Park J, Lee CS, Evans KA, McLaughlin EA, Pitman MR, Abbott CA, McCaughan GW et al. 2009. The in vivo expression of dipeptidyl peptidases 8 and 9. *The journal of histochemistry and cytochemistry : official journal of the Histochemistry Society* **57**: 1025-1040.

Yu DM, Wang XM, McCaughan GW, Gorrell MD. 2006. Extraenzymatic functions of the dipeptidyl peptidase IV-related proteins DP8 and DP9 in cell adhesion, migration and apoptosis. *The FEBS journal* **273**: 2447-2460.

Zhang H, Chen Y, Wadham C, McCaughan GW, Keane FM, Gorrell MD. 2015. Dipeptidyl peptidase 9 subcellular localization and a role in cell adhesion involving focal adhesion kinase and paxillin. *Biochimica et biophysica acta* **1853**: 470-480.

3

Acknowledgements

First of all, I would like to express my sincere gratitude to Dr. Iwona Ksiazek for giving me the opportunity to do my PhD in her lab and for being a great supervisor. I appreciate her tremendous support on the project and our valuable discussions. Without her guidance and input this thesis would not have been possible.

I would like to thank all the members of Dr. Ksiazek's group, Benjamin Küng, Delphine Weber, Berangere Gapp and Patrizia Barzaghi for their technical support as well as the fruitful discussions during the lab meetings. Especially I thank Benjamin Küng for the beautiful IHC images and his help in *in vivo* experiments. I am thankful to Dr. William Dietrich for constructive discussions and helpful advices.

I would also like to thank Prof. Antonius G. Rolink and Lilly von Münchow for their advices and critical feedbacks on the mouse immune-related phenotypes. We could not have performed fetal liver reconstitution assay without their technical support.

I am grateful to Prof. Filippo Rijli and his group members, Dr. Maryline Minoux, Nathalie Vilain and Dr. Ahmad Bechara for their input on mouse sensory system development. I appreciate our fruitful discussions and techniques which I have learned from them.

I thank Corrine Haller for the generation of DPP9 transgenic mice, and Johann Wirsching and Samuel Barbieri for their supports on molecular biology. I am thankful to laboratory animal service team, Martin van de Velde and Clara Kessler, for setting up the mouse time matings and maintaining the animal facility. I also thank Dr. Daniel Breustedt and Karla Rabsilber for the mouse genotyping.

I would like to thank Dr. Alessandro Piaia and Dr. Reginald Valdez for the histological evaluations and Dr. Kenji Namoto and Dr. Thorsten Lorenz for providing the activity based probe and introducing the activity based probe assay. I thank Thomas Le Meur for his assistance with the flow cytometry analysis.

I would like to thank Prof. Ed Palmer and Prof. Markus A. Rüegg for being members of my PhD committee and for the helpful and encouraging thesis committee meetings.

I thank Hyunwoo, Andrea, Rossa, Yujeong, Carole, Annabelle, Soobin, Swetlana, Cornelia and my family for supporting me during my study.